Geophysical Journal International

Geophys. J. Int. (2011) **187,** 303–326 doi: 10.1111/j.1365-246X.2011.05132.x

Multistep modelling of teleseismic receiver functions combined with constraints from seismic tomography: crustal structure beneath southeast China

Hrvoje Tkalčić,[1] Youlin Chen,[2] Ruifeng Liu,[3] Huang Zhibin,[3] Li Sun[3]
and Winston Chan[2]

[1] *Research School of Earth Sciences, The Australian National University, Mills Road, Building* 61, *Canberra* ACT 0200, *Australia.*
E-mail: Hrvoje.Tkalcic@anu.edu.au
[2] *Array Information Technology, Inc., Greenbelt, Maryland, USA*
[3] *Chinese Earthquake Network Center, China Earthquake Administration, Beijing, China*

Accepted 2011 June 28. Received 2011 May 16; in original form 2010 September 12

SUMMARY

With a growing number of modern broad-band seismographic stations in Asia, the conditions have improved to allow higher resolution structural studies on regional scales. Here, we perform a receiver-based study of the lithosphere of southeast China using waveform records of excellent quality from 14 Chinese National Digital Seismic Network and four Global Seismic Network stations. Calculating the theoretical receiver functions (RFs) that match the observed RFs from teleseismic waveforms is an established technique for retrieving information about crustal and upper mantle structure beneath a seismic receiver. RFs, however, are predominantly sensitive to the gradients in the lithospheric elastic parameters, and it is impossible to determine a non-unique distribution of seismic parameters such as absolute shear wave speeds as a function of depth unless other geophysical data are combined with RFs. Thus, we combine RFs with independent information from shear and compressional wave speeds above and below the Mohorovičić discontinuity, available from the existing tomographic studies. We introduce a statistical approach for automatically selecting only mutually coherent RFs from a large set of observed waveforms. Furthermore, an interactive forward modelling software is introduced and applied to observed RFs to define a prior, physically acceptable range of elastic parameters in the lithosphere. This is followed by a grid-search for a simple crustal structure. An initial model for a linearized, iterative inversion is constructed from multiple constraints, including results from the grid-search for shear wave speed, the Moho depth versus v_p/v_s ratio domain search and tomography. The thickness of the crust constrained by our multistep approach appears to be more variable in comparison with tomographic studies, with the crust thinning significantly towards the east. We observe low values of v_p/v_s ratios across the entire region, which indicates the presence of a very silicic crust. We do not observe any correlation between the crustal thickness or age of the crust with v_p/v_s ratios, which argues against a notion that there is a simple relationship between mineralogical composition and crustal thickness and age on a global scale.

Key words: Time-series analysis; Composition of the continental crust; Cratons.

1 INTRODUCTION AND MOTIVATION

1.1 Teleseismic receiver functions modelling

With an increasing volume of new instruments and data, it is becoming possible to resolve small-scale structural features worldwide, which enables the construction and further refinement of continental-scale or even global crustal models (e.g. Laske *et al.* 2000). Among other techniques, the teleseismic receiver functions (RFs) technique has been used routinely to estimate lithospheric structure. The rationale behind the RFs technique is taking advantage of repetitive waveform features of three-component seismograms and isolating the shear wave response of the crust and upper mantle beneath the recording station. The advantages and limitations of the technique are described in early papers (e.g. Langston 1979; Owens 1987; Owens *et al.* 1987; Ammon *et al.* 1990; Ammon 1991; Cassidy 1992). In practice, the deconvolution of an incident wave from the mode-converted wave could be done in both the frequency (e.g. Langston 1979; Owens *et al.* 1987; Ammon 1991; Park & Levin 2000; Helffrich 2006) and the time domain (e.g. Ligorría & Ammon, 1999; Julià *et al.* 2000). Furthermore, various transformations of coordinates have been used to determine structure from the inversion of teleseismic RFs, including those that minimize the initial *P*-pulse (e.g. Vinnik 1977; Kind *et al.* 1995; Reading *et al.* 2003)

While RFs are sensitive to gradients in seismic velocities, they are weakly sensitive to absolute velocities. Despite that, there are a large number of studies that use only RFs, and produce a first-order estimate of structural models of Earth, with parameters such as crustal thickness. Methods to model crustal structure with RFs have relied on forward modelling (e.g. Baker *et al.* 1996; Çakir *et al.* 2000; Zhu & Kanamori 2000), linearized inversion (e.g. Ligorría & Ammon 1999), grid-search (e.g. Sandvol *et al.* 1998) or a combination of approaches (Tkalčić *et al.* 2006). Similarly, RFs have been inverted using non-linear techniques such as the genetic algorithm (Shibutani *et al.* 1996), the neighbourhood algorithm (Sambridge 1999; Agostinetti *et al.* 2002), the microgenetic algorithm (Chang *et al.* 2004) and the niching genetic algorithm (Lawrence & Wiens 2004).

It has been shown, however, that if RFs are jointly inverted with surface wave dispersion, such an approach provides a better estimate of the overall velocity structure. This has been done in various parts of the world using various inversion techniques (e.g. Özalaybey *et al.* 1997; Du & Foulger 1999; Zhou *et al.* 2000; Julià *et al.* 2000, 2003; Chang *et al.* 2004; Lawrence & Wiens 2004; Pasyanos *et al.* 2007). In a recent study, we integrated grid-searches, linearized inversion and forward methods to a multiple step approach with the goal of jointly modelling observed broad-band long-period surface wave group velocity dispersion and teleseismic RFs for lithospheric structure including polarization anisotropy (Tkalčić *et al.* 2006).

Although the inversion methods have been widely used for modelling of RFs, we develop and use an interactive RFs forward modelling (IRFFM) software (Tkalčić & Banerjed 2009) that allows a quick assessment of different features seen in the observed RFs. Interactive modelling also allows us to explore a wide range of 1-D velocity models and get an intuitive insight on the acceptable elastic parameters in these models beneath each station.

Methods that use multiple geophysical data have the advantage of improved sensitivity to absolute velocities, compared to RFs alone. Here, we use RFs complemented with shear and compressional wave velocity information from independent tomographic models, mainly to increase constraints on absolute velocity and v_p/v_s ratio in the uppermost mantle. After the best fit to the observed RFs is found using a small number of free parameters from IRFFM and a simple grid-search, such model is combined with the tomography constraints to construct an initial model for a linearized inversion.

Our resulting structural models are thus in reasonable agreement with the models previously derived from tectonic and tomographic studies (e.g. Hearn & Ni 2000; Liang *et al.* 2004; Sun *et al.* 2004; Sun & Toksöz 2006; Ma & Zhou 2007; Chen *et al.* 2010) and with active-source seismic profiles in China (Li & Mooney 1998; Li *et al.* 2006), although they very likely improve the existing Moho depths from the teleseismic tomographic inversion, given the limitations of teleseismic tomography in vertical resolution. Our results confirm a complex tectonic setting, but yield a shallower crust–mantle discontinuity than inferred from previous tomographic studies. This will be important for the interpretation of lithospheric processes on a wider scale, when the seismic profiles from the surrounding countries become available.

1.2 Area of study and waveform data

One of the countries that have invested significant efforts in expanding its seismic networks, assisted primarily through its own governmental funds is China. The Chinese National Digital Seismic Network (CNDSN) consists of 48 three-component permanent broad-band stations across China. Digitally recorded waveform data are transferred in real time to the China Earthquake Network Center (CENC) through satellites. Due to the vast area of Asia that China covers, such effort yielded favourable conditions to improve the understanding of the tectonic settings and, more generally, the identification of crustal and upper mantle physical and chemical properties in a number of inadequately studied regions. One such understudied region is the southeastern part of China and the territory immediately to the southeast, belonging to Vietnam, Laos and Cambodia.

From a geological perspective, our study region focuses on north and south China blocks (Fig. 1). The North China Block (NCB) is also known as Sino-Korean Craton; whereas the South China Block (SCB) consists of the Yangtze Craton and the Cathaysia Block. The Cathaysia Block comprises the South China Fold Belt and an underwater section to the east. Although NCB and SCB both have Archean basements, they underwent substantial internal deformation over the course of their Phanerozoic history. The SCB first collided with the NCB during the late Permian, initially in the east, and progressively migrated westward along the Qinling-Dabie–Sulu suture zone in the Triassic (Yin & Nie 1996). The collision occurred as a northward underthrusting of the SCB under the NCB, and very likely it led to the uplift in the north of the Sulu and Qinling-Dabie orogens, and the flexural subsidence of the southern zones (Vermeesch 2003). During the Mesozoic and Cenozoic, intracontinental deformation was widespread in both south and north China as a few reactivations of Palaeozoic fold belts formed complicated systems of intracontinental mountain ranges and sedimentary basins. One example is the development of widespread extensional basins (roughly corresponding to the Huabei Plateau) throughout the NCB during the Mesozoic caused by horizontal extension of previously thickened crust (Wang *et al.* 2005). The rifting and extension of the western part of the Pacific Ocean generated a series of extensional faults and rifted basins in the eastern part of the Yangtze Craton and the South China Fold Belt. The boundary between the Yangtze and the Cathaysia blocks is poorly documented due to the lack of detailed data to better constrain its suture. The general distinction between these two regional blocks was proposed on the basis of dissimilarities in the stratigraphic records (Ji & Coney 1985) and the possible occurrence of ophiolite suites (Zhang *et al.* 1984).

We select 18 available stations from the southeastern part of China to perform the comprehensive point measurements of lithospheric structure properties under each receiver site. These 18 stations are evenly spanning over all tectonic blocks in the southeast China (Fig. 1). Specifically, we have three stations on the Sino-Korean Craton, two stations along the Qinling-Dabie Fold Belt, seven stations on the Yangtze Craton and six stations across the South China Fold Belt. In addition, we attempted to analyse station XSA from the underwater section of the Cathaysia Block (shown in Fig. 1), but

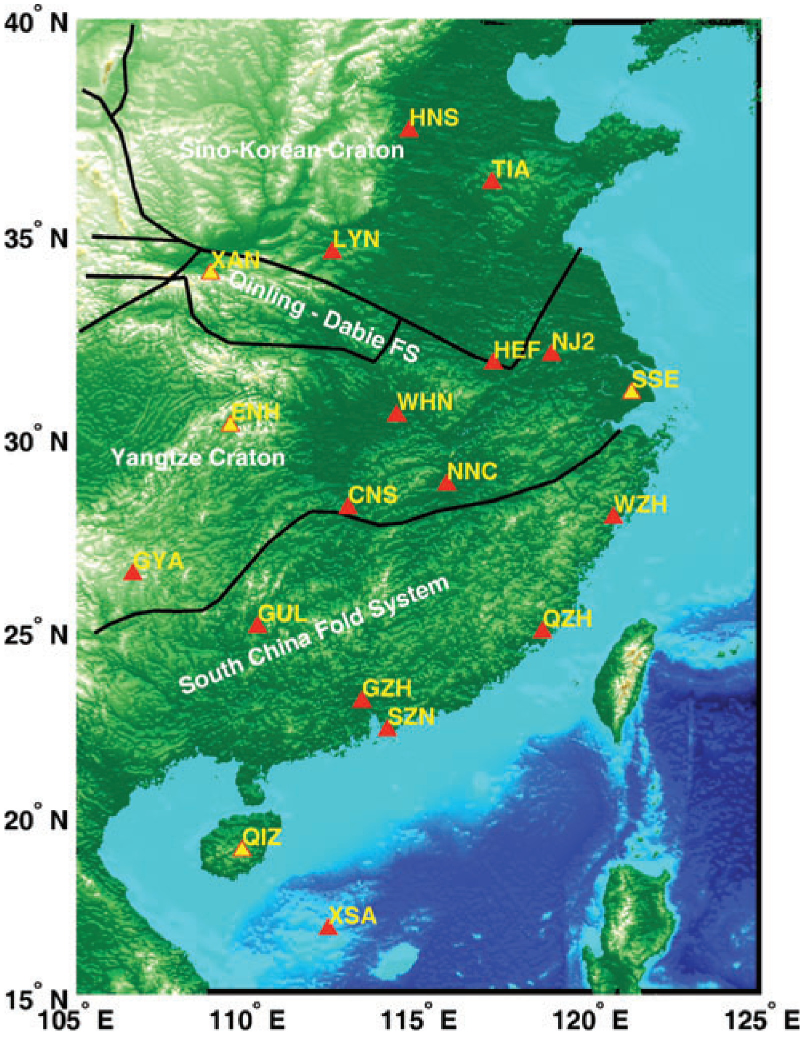

Figure 1. Topographic map of the southeastern part of China and surroundings with the distribution of CNDSN (red triangles) and four GSN stations (yellow triangles) selected for this study.

the results were not taken into account due to poor signal-to-noise ratio.

2 MULTISTEP METHOD AND PROCESSING OF RECEIVER FUNCTIONS

2.1 Pre-processing of raw waveforms

Fig. 2 illustrates 5 yr (2001–2005) global seismicity with $M_b \geq 5.9$. There are 350 teleseismic events recorded at the CNDSN stations satisfying this criterion. We chose the events whose epicentral distances are confined between 30° and 90° to secure near-vertical incidence of the *P* waves. Most seismicity that occurred at distances suitable for the RFs technique is confined around the Kuril Islands in the north, and the Indonesia and Tonga-Fiji regions in the southeast. There is also a group of earthquakes that occurred in the Mediterranean region, resulting in the western backazimuths, and the Indian and the South Atlantic Oceans with southwestern azimuths. Because a single station collects a large number of potentially useful teleseismic events, at this stage we did not perform a strict data-quality control on the raw waveforms, apart from the criterion that their M_b is larger than 5.9. However, we removed the mean and trends, and applied a high-pass filter to eliminate long-period fluctuation ($T >$ 15 s). We then produced shorter time-series concentrated around the first arrival by cutting traces at 5 s prior to and 30 s after the initial *P*-wave arrival. Finally, horizontal components were rotated to radial and tangent directions before the deconvolution.

The distribution of the 18 stations used in this study is shown in Fig. 1. As expected, we encountered some problems in the data pre-processing stage. For example, some stations had undergone location changes in the period from 2002 to 2004, and this had to be taken into account in calculating relevant parameters for RFs, as well as kept in mind for the time when interpreting seismological structure below stations. Broad-band data for Global Seismic Network stations are available through IRIS (Incorporated Research Institutions for Seismology) acquisition system and we included them in this study. Most stations revealed excellent data quality. For occasionally low signal-to-noise ratio, waveforms that result in a poorer quality RF but the abundance of available data can somewhat compensate the lack of quality. The only station with significantly poorer quality data than recorded at other stations is XSA, located at the Xisha Islands (Fig. 1).

Fig. 2 focuses on the selected 18 stations and shows locations of global earthquakes with M_b larger than 5.9. We divide waveform

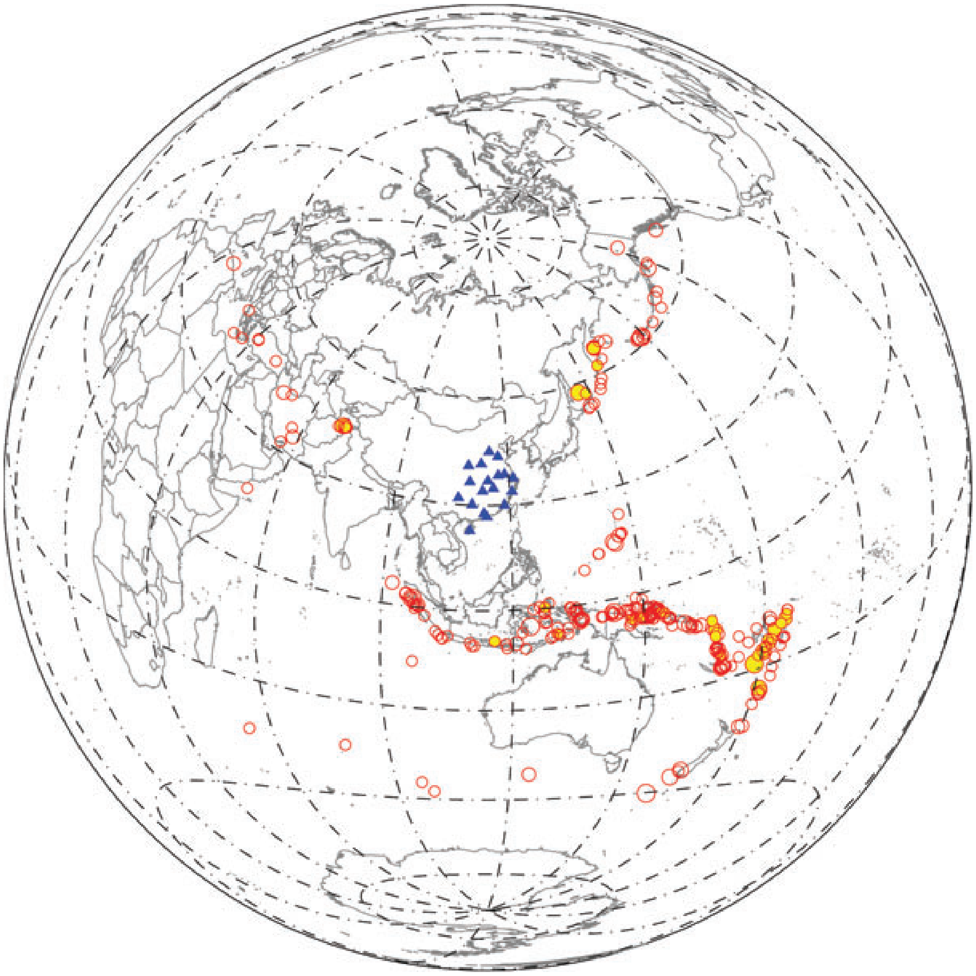

Figure 2. Global distribution of $M_b \geq 5.9$ earthquakes for the period 2001–2005. Red triangles are stations shown in Fig. 1. About 80 per cent of the teleseismic events are recorded at CNDSN stations with high signal-to-noise ratio.

data in the reference frame of each station based on their directions of sampling (backazimuth of their incoming energy) to four major groups. The division to four quadrants (each quadrant corresponds to 90° bandwidth of the backazimuthal range) was determined empirically upon the RFs analysis on several stations, when we noticed that RFs within each quadrant do not vary significantly in their character. Ideally, we expect the resulting RFs for each subdivision to show a high level of coherency. In general, for the analysed stations, we obtained systematically poorer in quality, and less in number RFs for data corresponding to the third quadrant (southwestern backazimuths). The most abundant data correspond to the second quadrant (southeastern backazimuths). In Fig. 3, we highlight the paths in the second quadrant, associated with the earthquakes originating in the southwestern part of the Pacific for station GUL. This particular range of backazimuths and distances was chosen after some trial-and-error as it provided enough data of high quality on all stations. By choosing only one azimuthal range with a narrow interval of ray parameters, we have set the issues in conjunction with a possible Moho dip and anisotropy aside, however we evaluate that the azimuthal variation is less significant in the context of meeting our goal of constructing 1-D models of the crust and upper mantle compatible with multiple geophysical data sets.

We chose an iterative deconvolution procedure in the time domain, the method that does not require selecting water level in frequency domain (Ligorría & Ammon 1999) to calculate RFs at each station. This method performs well, and has been adopted as a method of choice in a number of recent studies (e.g. Julià *et al*. 2000; Tkalčić *et al*. 2006; Chen *et al.* 2010) despite a slightly longer computer-running time.

2.2 RF selection using the cross-correlation matrix method

Resulting radial RFs for each station could be routinely stacked and averaged for a number of earthquakes from several backazimuths. To increase the efficiency of processing a large number of waveforms, we first calculate RFs from all available waveforms for a given station and an azimuth range forming a bundle. When processing small to moderate number of RFs, it is appropriate to select waveforms by visual examination for their coherency corresponding to *P–S* conversions, and careful elimination of outliers and noisy records. However, when working with a large number of RFs in a bundle, such as the one considered here, one can benefit from the large quantity of data, but it becomes challenging to justify a visual selection of waveforms for stacking. A more sophisticated approach is by all means necessary to make a selection of coherent RFs from our large data set. One cannot rely on the signal-to-noise ratio estimates only, because in cases where the first arrivals are misidentified, the signal-to-noise ratio might still be favourable, but

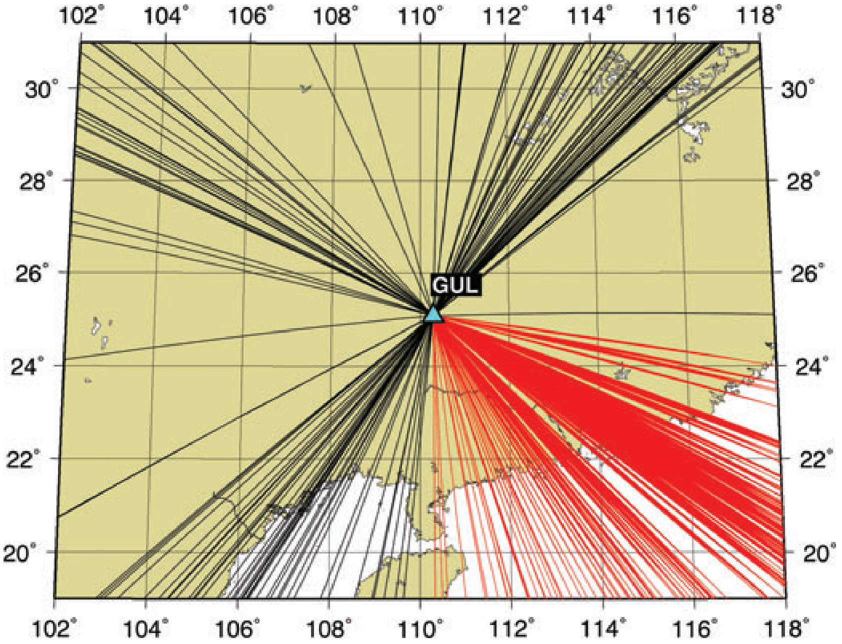

Figure 3. A close-up of the location of station GUL, with surface projections of ray paths corresponding to all available waveforms for the period of study. Highlighted in red are ray paths predominantly from the Tonga-Fiji region in the Pacific Ocean within the 90°–180° backazimuth range.

the corresponding waveform is different from the rest of the waveforms in a sample. The *ad hoc* determination of which waveforms are outliers and thus should be discarded prior to stacking is not desirable. A subjective selection of waveforms for stacking can result in an averaged waveform that is distorted or lacking some representative features, especially at the later times where the signals from the changes in crustal properties are weaker. Therefore, a special care should be taken in selecting only mutually coherent waveforms in a statistical fashion, especially in cases where we have the luxury of working with a large number of waveforms.

Let M represent the total number of RFs in a bundle with a similar ray parameter, and $\{r_i(A_k,t_k), r_j(B_k,t_k), i = 1 \ldots M; j = 1 \ldots M; k = 1 \ldots N\}$ any two selected time-series (RFs) with N samples and amplitudes A_k and B_k. A cross-correlation matrix of the following form can be constructed:

$$\begin{bmatrix} r_{11} & r_{12} & \cdots & r_{1j} & \cdots & r_{11} \\ r_{21} & r_{22} & & & & \\ \vdots & & \ddots & & & \\ r_{i1} & & & r_{ij} & & r_{iM} \\ \vdots & & & & \ddots & \\ r_{M1} & r_{M2} & \cdots & r_{Mj} & \cdots & r_{MM} \end{bmatrix}, \qquad (1)$$

where r_{ij} are the cross-correlation coefficients between two RFs. The diagonal elements ($i = j$) are zero-lag cross-correlation coefficients equal to one, corresponding to the comparison of a RF to itself (autocorrelation functions). The matrix is symmetric with r_{ij} equal to r_{ji}. (A note to Seismic Analysis Code users: the cross-correlation coefficients r_{ij} calculated using the command 'correlate' require the normalization by square roots of the autocorrelation functions for r_i and r_j in order to return coefficients between 0 and 1.)

The cross-correlation matrix provides a way of conveniently comparing correlations, which is not dependent on the units of the original data, and which has the same upper and lower bounds. As an independent control parameter, matrices of variance reduction (VR) and root mean square (rms) for each pair of RFs are also calculated (we use the same definitions as in Tkalčić *et al.* 2006).

We designed an algorithm that has two stages: (1) it computes the matrices described earlier and (2) it selects only those waveforms that satisfy the following criteria: for a single RF $r_i(A_k,t_k)$, the cross-correlation coefficients with other RFs $r_j(B_k,t_k)$ must be higher than some predetermined value χ. This has to be satisfied for a given percentage τ of all RFs from the bundle. Hence, the algorithm extracts only those rows of the cross-correlation matrix in which cross-correlation coefficients exceed given threshold value χ of the cross-correlation coefficient in τ per cent out of M cases. We determine τ and χ empirically, using the trial-and-error approach. The values $\chi = 0.9$ and $\tau = 25$ per cent in cases when the number of waveforms is larger than 50 (the majority of cases) and $\tau = 10$ per cent in cases when the number of waveforms is smaller than 20 proved to work very well. Naturally, the higher the threshold cross-correlation coefficient χ and the percentage τ, the lower the final number of RFs that will satisfy the coherency criteria. For $\tau = 0$ per cent, all RFs would be selected as 'coherent'.

The approach described earlier works well when the number of waveforms is large: the method will discover one or more different, but mutually coherent waveform groups within the same bundle. It is especially suitable to identify mutually coherent waveforms in bundles consisting of noisy RFs that were conservatively not rejected in the pre-processing stage. We tested algorithms where the mean was calculated first, and the coherency among waveforms was attempted to be deduced by comparing each waveform with the mean, but this approach did not yield desired results because the mean could be very biased by noisy waveforms.

As an example, the selection results for station GUL are plotted in Fig. 4, where all calculated RFs are plotted in black and the mutually coherent RFs selected by our algorithm are plotted in blue. The thick red line is an average of the selected RFs. Fig. 4(a) shows the resulting coherent RFs with a less strict selection criterion (each

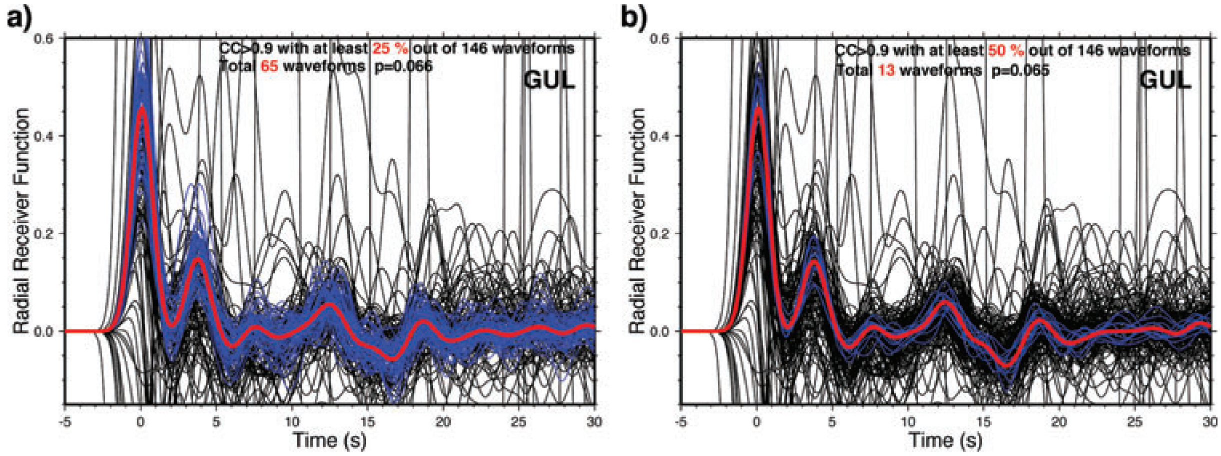

Figure 4. Radial RFs calculated for station GUL from the southeastern quadrant (highlighted in Fig. 3) for all earthquakes without rejecting waveforms based on signal-to-noise ratio are shown in black. Mutually coherent waveforms selected using the cross-correlation matrix approach are shown in blue. The selected waveforms are correlated with the cross-correlation coefficient 0.9 or higher with (a) at least 25 per cent of other waveforms and (b) at least 50 per cent of other waveforms. The thick red line is the average calculated from the selected RFs.

waveform correlates with $\chi = 0.9$ or higher with at least $\tau = 25$ per cent of other waveforms), whereas Fig. 4(b) shows the resulting RFs with a more strict selection criterion (each waveform correlates with $\chi = 0.9$ or higher with at least $\tau = 50$ per cent of other waveforms). Although the number of selected waveforms reduces drastically for $\tau = 50$ per cent, the averaged RFs looks very similar in both cases. This demonstrates that the final RF is less dependent on our empirical subjective selection of statistical criteria. Similarly, when the threshold cross-correlation coefficients are reduced to $\chi = 0.8$, the resulting RF does not change significantly.

2.3 Crustal thickness and v_p/v_s ratio

Most inversion methods to crustal velocity require a fixed Moho depth in advance. Moreover, the crustal thickness, as well as v_p/v_s ratio and hence Poisson's ratio are important objectives in this study. The Moho depth can be estimated from the time difference between the initial *P*-wave arrival and that of the converted phase *Ps* at Moho. One problem of this method is the trade-off between the crustal thickness and velocities, but that can be reduced by the consideration of the crustal multiple phases that follow. In this study, we adopted an advanced H--κ (crustal thickness–v_p/v_s ratio) domain stacking and search procedure (Niu *et al.* 2007; Chen *et al.* 2010) to estimate the crustal thickness and v_p/v_s ratio simultaneously. The stacking function is defined as

$$s(H,\kappa) = \frac{c(\kappa)}{N}\sum_{i}^{N}[\omega_1 r_i(t_1) + \omega_2 r_i(t_2) - \omega_3 r_i(t_3)], \qquad (2)$$

where N is the number of RFs at a given station, $c(\kappa)$ is semblance of the three traces around the peak of the *Ps* trace, $r_i(t)$ represents the amplitude of the ith RF at the predicted arrival times of the primary *P*-to-*S* converted phase *Ps*, and crustal multiples *PpPs* and *PpSs*+*PsPs*, respectively. Considering the negative polarity of both phase modes *PpSs* and *PsPs*, we assign to it a negative sign in the summation. ω_1, ω_2 and ω_3 are the weighting factors, requiring $\sum \omega_i = 1$and $\omega_1 \geq \omega_2 + \omega_3$. This stacking technique has the advantage of efficiently processing large amounts of RF traces without manually picking arrival times of any conversion phases. More importantly, it correctly calculates the moveouts of the *P*-to-*S* phase and Moho reverberation phases, which consequently leads to a constructive stacking of the three phases.

From many previous studies using this technique (e.g. Zhu & Kanamori 2000; Chevrot & van der Hilst 2000; Niu & James 2002; Nair *et al.* 2006), however, we found that simple summation for the three phase modes with different weighting factors could not completely remove the trade-off effect between crustal thickness and v_p/v_s ratio. It usually leads to a large 'band' area in the H–κ domain contour, in which multiple local maxima of RFs amplitude peaks that correspond to different crustal thickness and v_p/v_s ratio combinations can be found. In order to make the H–κ search more effective, we calculated the coherence between the *P*-to-*S* converted phase and crustal multiples at different κ values, and applied their semblance, $c(\kappa)$ featured in eq. (2), as an additional weighting factor. If the assumed κ is correct, the three depth traces are expected to correlate well with each other around the maximum conversion depth.

We demonstrate the efficiency of the algorithm for station GUL, for which we assign the average crustal *P*-wave velocity of 6.19 km s^{-1} as in an independent tomographic study for China (Sun & Toksöz 2006). The H–κ domain is searched from 20 to 90 km for crustal thickness and from 1.50 to 2.00 for v_p/v_s ratio. The function $s(H,\kappa)$ is plotted in Fig. 5, and its maximum value corresponds to $H = 30.6 \pm 0.3$km and $\kappa = 1.718 \pm 0.007$. The range of RFs used in this method is plotted in Figs 8–10.

2.4 Interactive forward modelling of RFs

The IRFFM is a Java program written for interactive forward modelling of RFs (Tkalčić & Banerjed 2009) that is made freely available on the Internet. It is a useful complement to the inversion or a standalone tool. An easy-to-use graphic interface is designed to enable the user to efficiently manipulate with thicknesses and velocities, as well as v_p/v_s ratios in a 1-D model of Earth. It quickly displays the theoretical and the observed RFs and reveals how the 1-D model has to be changed to reduce their misfit. Input RF is in a two-column *ascii* format. Input velocity models are also in *ascii* format, and two starting models are provided with the package (ak135 and PREM). The users can use one of these two models as a starting model, construct their own from other geophysical constraints or simply guess an initial Earth structure. It is possible to save current model at

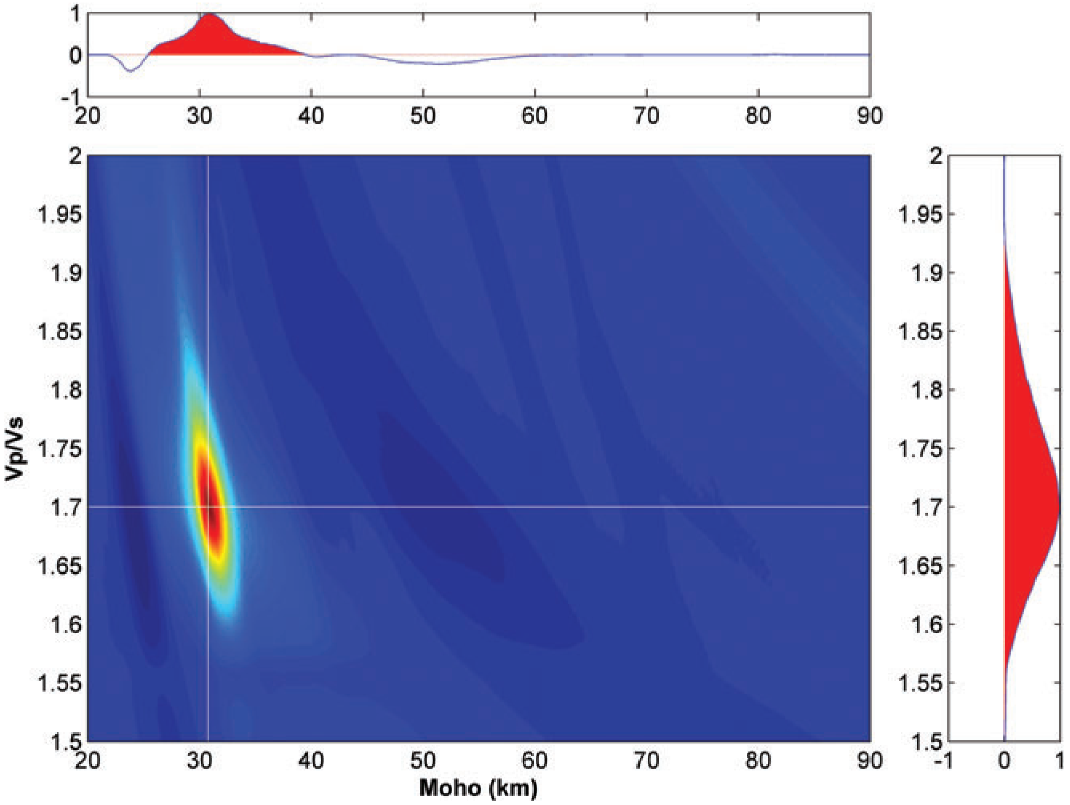

Figure 5. $s(H, \kappa)$ domain search from radial RFs for station GUL, using the approach from Niu *et al.* (2007) and Chen *et al.* (2010). The best estimate of the crustal thickness is 30.6 km with a v_p/v_s ratio of 1.72.

any time during the forward modelling for the future use or upload another observed RF at any time.

The method used in IRFFM for the calculation of the theoretical RFs consists of the synthetic seismogram algorithm by G. Randall (*respknt*), based on the method developed by Kennett (1983) and a time-domain deconvolution to produce synthetic RFs in the same manner as it is done for the observed RFs (*iterdecon*). Therefore, the program is closely tied to the time-domain iterative deconvolution procedure described by Ligorría & Ammon (1999), and on the homepage of Ammon (http://eqseis.geosc.psu.edu/∼cammon/). Currently available Gaussian filters are $a = 1.0$, 2.5, 5.0 and 10.0.

We used IRFFM to get a quick understanding of the features present in RFs, as well as a quantitative measure about the range of parameters that produce theoretical RFs similar to the observed RFs. For example, one can explore how the crustal thickness and the impedance contrast affect the P-to-S conversion, seen as the second peak in observed RFs. A screenshot with the IRFFM user interface is shown in Fig. 6. This figure illustrates how Earth structure is modelled using only three layers of different thicknesses and velocities in the crust and a half-space in the mantle to fit observed RF at station GUL. In this example, v_p/v_s ratio along the profile is kept constant, although it can be variable. The parameter space that is determined this way, along with the results for other stations, is used as *a priori* information for a grid-search that explores structural models of Earth in a systematic way. The estimated model parameters using IRFFM are in a good agreement with the results from the H–κ search shown in Fig. 5. IRFFM is available for download from the following Internet address: www.rses.anu.edu.au/∼hrvoje/IRFFM.html.

2.5 Grid-search for the first-order lithospheric structure

Armed with the initial estimates from the H–κ method and forward modelling for each of the 18 stations, we further improve our results using a grid-search. A critical advantage of a grid-search method over other inversion techniques is that it provides the goodness-of-fit statistics for the entire parameter space, within the limitations of its discrete nature. This is advantageous in situations where not even an approximate structure under a station is known *a priori*. A disadvantage of grid-search methods lies in the fact that they are computationally intensive, especially in the context of jointly inverting several independent data sets. Because the structure of the parameter space might be finer than the selected grid spacing, some assumptions are required in order to simplify the problem.

We simplify the problem of finding the best RFs fit, reducing the inverse problem to three or four layers in the crust and an additional layer below the crust extending to the depth of 80 km. To create structural models for long enough RF synthetics, below 80 km we use a series of layers with thicknesses and velocities from PREM (Dziewonski & Anderson 1981). We first impose minimal *a priori* constraints on the crustal thickness from forward modelling described in the Section 2.4, typically allowing it to vary between 24 and 48 km. This thickness is also well within an interval of crustal thicknesses predicted by an independent study from tomography (Liang *et al.* 2004; Sun & Toksöz 2006) and from the H–κ method (Chen *et al.* 2010).

The resulting models have only three layers in the crust and a relatively coarse grid (gridpoints at 2 km for surface layer thickness, at 3 km for other layers and 0.2 and 0.3 km s^{-1} for shear

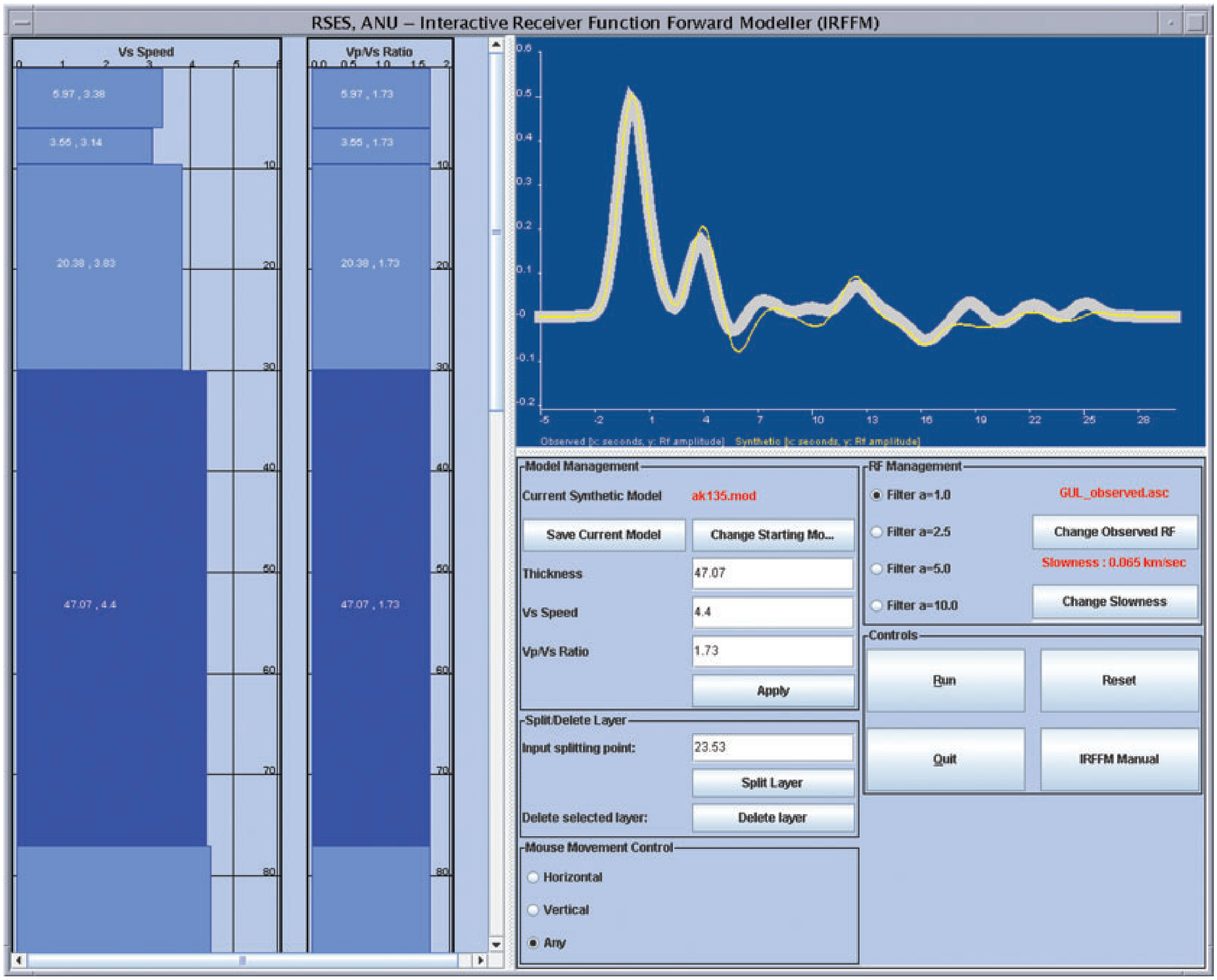

Current Synthetic Model ak135.mod

Thickness 47.07

Vs Speed 4.4

Vp/Vs Ratio 1.73

Input splitting point: 23.53

Delete selected layer:

○ Horizontal
○ Vertical
● Any

● Filter a=1.0
○ Filter a=2.5
○ Filter a=5.0
○ Filter a=10.0

GUL_observed.asc

Slowness : 0.065 km/sec

Figure 6. Interactive receiver function forward modeller (IRFFM) interface, used to infer initial 1-D models of Earth for station GUL, compatible with the observed receiver function. Three layers in the crust were modelled for thickness and v_s velocity, keeping v_p/v_s ratio 1.73, compatible with the results shown in Fig. 5.

Table 1. Grid-search scheme used in the study, with flexible depth of the Moho defined between 24 and 48 km.

Layer	Thickness (km)	v_s (km s^{-1})	Δh (km)	Δv (km s^{-1})
1	$H_1 = 2\text{–}6$	$V_1 = 2.8\text{–}3.4$	2	0.2
2	$H_2 = 3\text{–}H_{\mathrm{Moho}} - (H_1+H_3+H_4)$	$V_2 = 3.2\text{–}3.6$	3	0.2
3	$H_3 = 3\text{–}\mathrm{H}_{\mathrm{Moho}} - (H_1+H_2+H_4)$	$V_3 = 3.4\text{–}3.8$	3	0.2
4	$H_4 = 3 - \mathrm{H}_{\mathrm{Moho}} - (H_1+H_2+H_3)$	$V_4 = 3.6\text{–}4.5$	3	0.3
5	$H_5 = 80 - H_{\mathrm{Moho}}$	$V_5 = 4.4\text{–}4.6$	–	0.1

wave velocity intervals depending on the depth of the layers). Upon initial inspection of the results from a coarse grid-search, we refine grid-search to four layers in the crust and an additional layer in the mantle extending to the depth of 80 km. The grid specifications are shown in Table 1. We assume Poisson's ratio of $\sigma = 0.25$ (this assumption could be modified based on other empirical results, as well as a trial-and-error approach) and the Birch's law for density (Birch, 1961). The number of free parameters for four crustal layers and one mantle layer is $2n+1 = 9$, where n is the number of layers (2 stems from shear wave velocity and thickness of each layer and 1 stems from shear wave velocity of the layer below the crust). We compute and store a database of synthetic RFs from a number of models according to the scheme above. This results in 482 976 synthetic RFs for each ray parameter. To compute synthetic RFs, we use the same method as in the forward approach with IRFFM. This is done for RFs with the Gaussian filter-width parameter $a = 1.0$ and the duration of 30 s, for a range of ray parameters.

As a measure of misfit, VR for each model is calculated according to the following expression:

$$VR = \left\{ 1 - \sqrt{\frac{\sum_i (d_i - m_i)^2}{\sum_i d_i^2}} \right\} 100\%$$

In the above expression, *d* and *m* are the observed and predicted values for RFs, respectively. Apart from the expression above, we also calculate cross-correlation coefficient and rms, as well as the weighted variance reduction VRw, where w is defined as 1/*A* (*A* is the maximum amplitude of the observed RF). The weight enters the above formula as a factor within the summation in both numerator and denominator. When numerically estimating the best models, both the cc and VR values are used as criteria.

The grid-search results are shown in Fig. 7 for all stations. The best 1000 models and the explored grid are shown on the right, with a logarithmic colour scheme emphasizing the best 10 models. Synthetic RFs for these 10 best models are also shown and compared to the observed RF for each of the selected stations. While we believe that the models obtained here are already a good representation of average crustal structure in terms of velocity gradients, it is important to take into account other constraints when deriving final velocity models.

2.6 Selection of starting model for linearized inversion from multiple constraints

To select a robust starting model for the inversion, one can focus on matching amplitudes and character of the first (direct *P*) and the second peak (*Ps*), as well as the later cycles (*PpPms* and *PpSms*+*PsPms*), which are sensitive to the velocity contrast at Moho. However, absolute velocities from previous tomographic studies, the *H*–κ domain search and the grid-search for simple structure are all excellent independent constraints that should be taken into account when constructing a starting model.

This is how the starting model is constructed for each station.

(1) Thickness and v_s velocity of crustal layers is taken from the grid-search results as the basis for the starting model. This model always contains four layers in the crust and a half-space in the mantle.

(2) v_p/v_s ratio in the crust is taken from the *H*–κ domain search.

(3) v_s in the upper mantle is not well constrained by the grid-search as there is a number of models with different v_s values in the upper mantle producing similar fit to observed RFs. Therefore, we select a model from the grid-search whose v_s is the most similar to the point value closest to the station from the v_s tomography model by Pei *et al.* (2004).

(4) v_p/v_s ratio in the mantle is then calculated from the point values closest to the station from tomographic models for *P*-wave velocity (Sun & Toksöz 2006) and *S*-wave velocity (Pei *et al.* 2004).

2.7 Linearized inversion for a detailed lithospheric structure under southeast China

In this step, we choose the model from multiple constraints described in the Section 2.6 as a starting model for a linearized, iterative inversion. We thus avoid a bias towards an unrealistic starting model, which is often the case where there are no *a priori* geophysical constraints. The linearized, iterative inversion will inevitably increase the number of model parameters thus sacrificing the simplicity of the initial structural models, yet it will significantly improve RFs fits at short periods. We use the algorithm developed by Ammon (1997), which is based on a singular value decomposition to compute the matrix inverse and solve the inverse problem. The algorithm allows using smoothness parameters to find the smoothest solution in the vicinity of the initial model that fits the data.

2.8 Selection of preferred model

Although increasing the number of free parameters in the linearized, iterative inversion enables us to fit different features in the observed RFs, we do not want to overparametrize our model space by unnecessary large number of layers. We conduct a simple grid-search, varying the number of iterations and the smoothness parameter in the inversion for different combinations of layers. Fig. 8 illustrates results of one such grid-search for station CNS, where VR is shown in the smoothness–iteration space for (a) four, (b) eight, (c) 10 and (d) 12 layers considered in the model. There is a drastic improvement in VR when increasing the number of layers from four to eight, much less improvement when going from 8–10 layers and literally no improvement when increasing the number of layers to 12. Therefore, the saturation in VR improvement for the waveforms from station CNS occurs when the number of layers is about 10. By repeating this procedure for each station, we choose to select an ensemble of models with three different combinations of the number of layers (below the saturation of VR point), for smoothness parameters 0.1, 0.2 and 0.3 and for iterations from 10 to 50, to represent models with a good fit. This process results in 360 models for each station. These models are shown by orange in Figs 9–11. The preferred model is then computed as an average of all models in an ensemble. Because Earth layers are of various thicknesses and their borders are positioned at different depths, in order to compute the average of velocity profiles, we further discretize layers to 1 km thickness. The preferred models (shown in red colour in Figs 9–11) are arithmetic means and appear as models consisting of a large number of layers of 1 km thickness. However, it is important to stress out that the large number of layers is not a result of an overparametrization in the model space, but a result of our final representation of preferred models.

Naturally, a single model from an ensemble might be the best-fitting model, however it is not necessarily the best physical model. Preferred models do not produce the best fits to the observed RFs, but are a much better representation of realistic Earth structure. See Figs 9–11 to compare how RFs from the best-fitting model compare to those computed from the preferred model. In most cases, they are very similar.

3 LITHOSPHERE BENEATH SOUTHEAST CHINA

3.1 Results

We organize the results of our multistep modelling into the three major tectonic and physiographic regions (Fig. 1). Four stations (HNS, TIA, LYN and XAN) are assigned into the Sino-Korean Craton, eight stations (NJ2, SSE, HEF, WHN, NNC, ENH, CNS and GYA) are located in the Yangtze Craton and six stations (WZH, QZH, GZH, SZH, GUL and QIZ) are included in the South China fold system. We have to note here that such division is somewhat arbitrary, and for the convenience of discussion. For instance, XAN

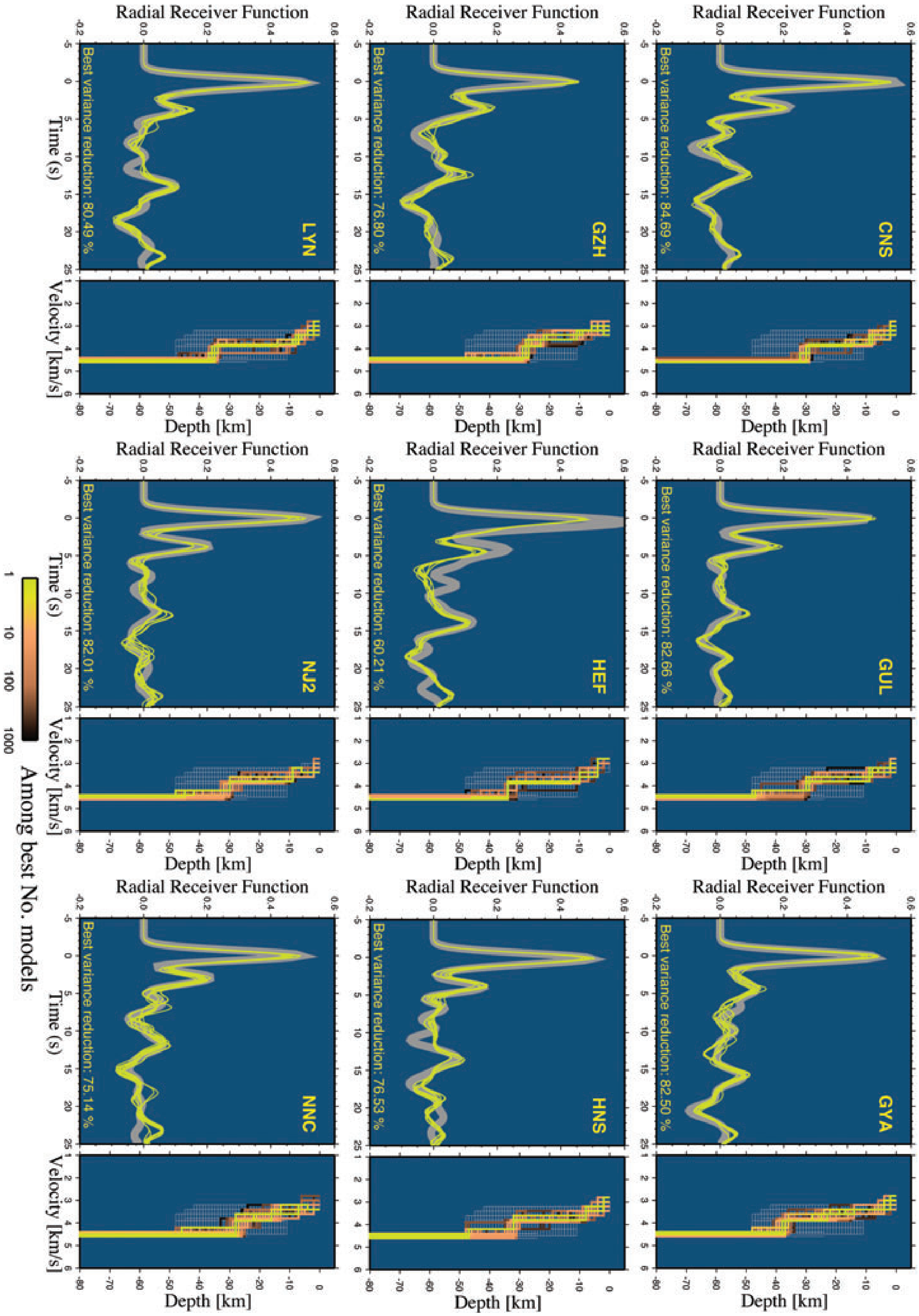

Figure 7. Grid-search inversion results (for four layers in the crust and a half-space in the uppermost mantle, according to Table 1 for 1-D v_s velocity structure at stations CNS, GUL, GYA, GZH, HEF, HNS, LYN, NJ2 and NNC). The observed RFs are shown with thick grey lines, and the synthetic RFs from the best 10 models are shown with yellow thin lines. Best-fitting 1000 models are displayed on the right side using the logarithmic colour scheme. PREM is indicated with black thick lines. Compare fits for GUL with Fig. 6. (Continued) Grid-search inversion results for 1-D v_s velocity structure at stations QIZ, QZH, SZN, TIA, WHN, ENH, SSE, WZH and XAN.

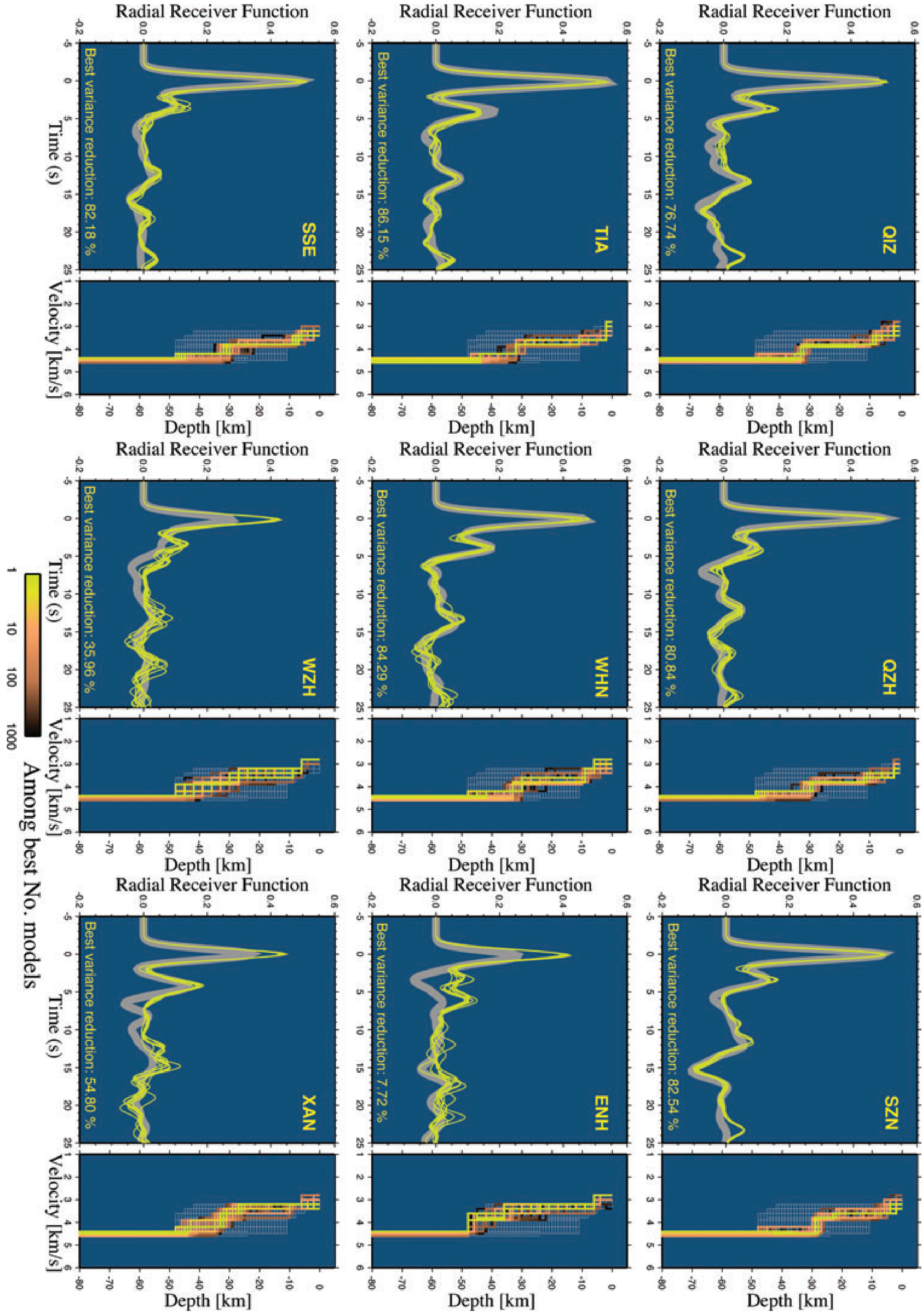

Figure 7. (*Continued.*)

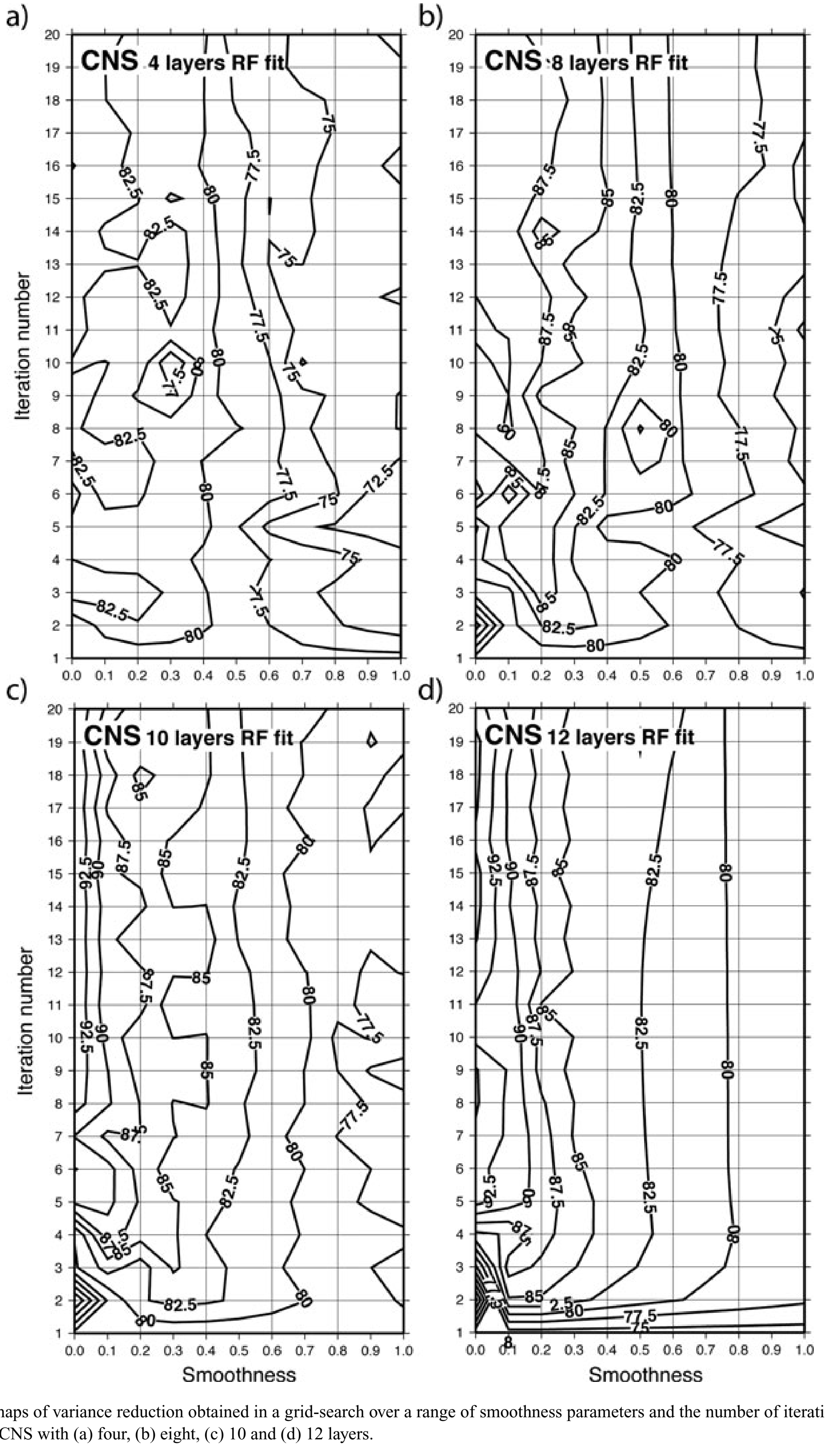

Figure 8. Contour maps of variance reduction obtained in a grid-search over a range of smoothness parameters and the number of iterations in the linearized inversion for station CNS with (a) four, (b) eight, (c) 10 and (d) 12 layers.

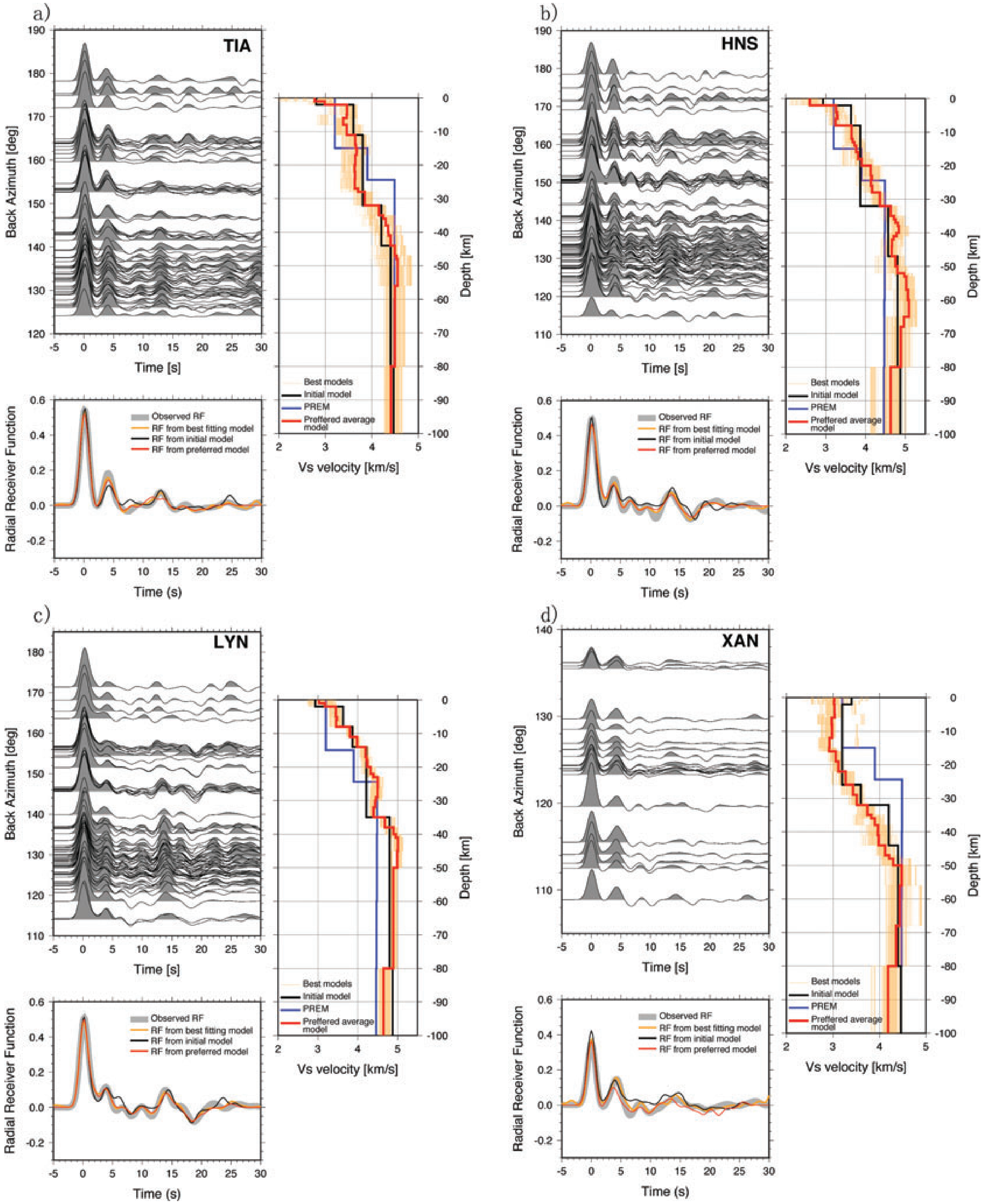

Figure 9. Results from the linearized inversion of RFs (shown for each station as a function of backazimuth in the upper left corner) for the Sino-Korean Craton: (a) TIA, (b) HNS, (c) LYN and (d) XAN. Grey thick lines (shown in the lower left corner) are the observed RFs, whereas thinner lines in different colours correspond to the synthetic RFs from the inverted velocity profiles shown on the right side, and explained in the legends. The initial model (obtained from multiple constraints including the H–κ method, tomography and grid-search) is shown in black, whereas PREM is shown in blue. The best fitting models are in orange and their average is in red. Station order is in decreasing distance from the coast.

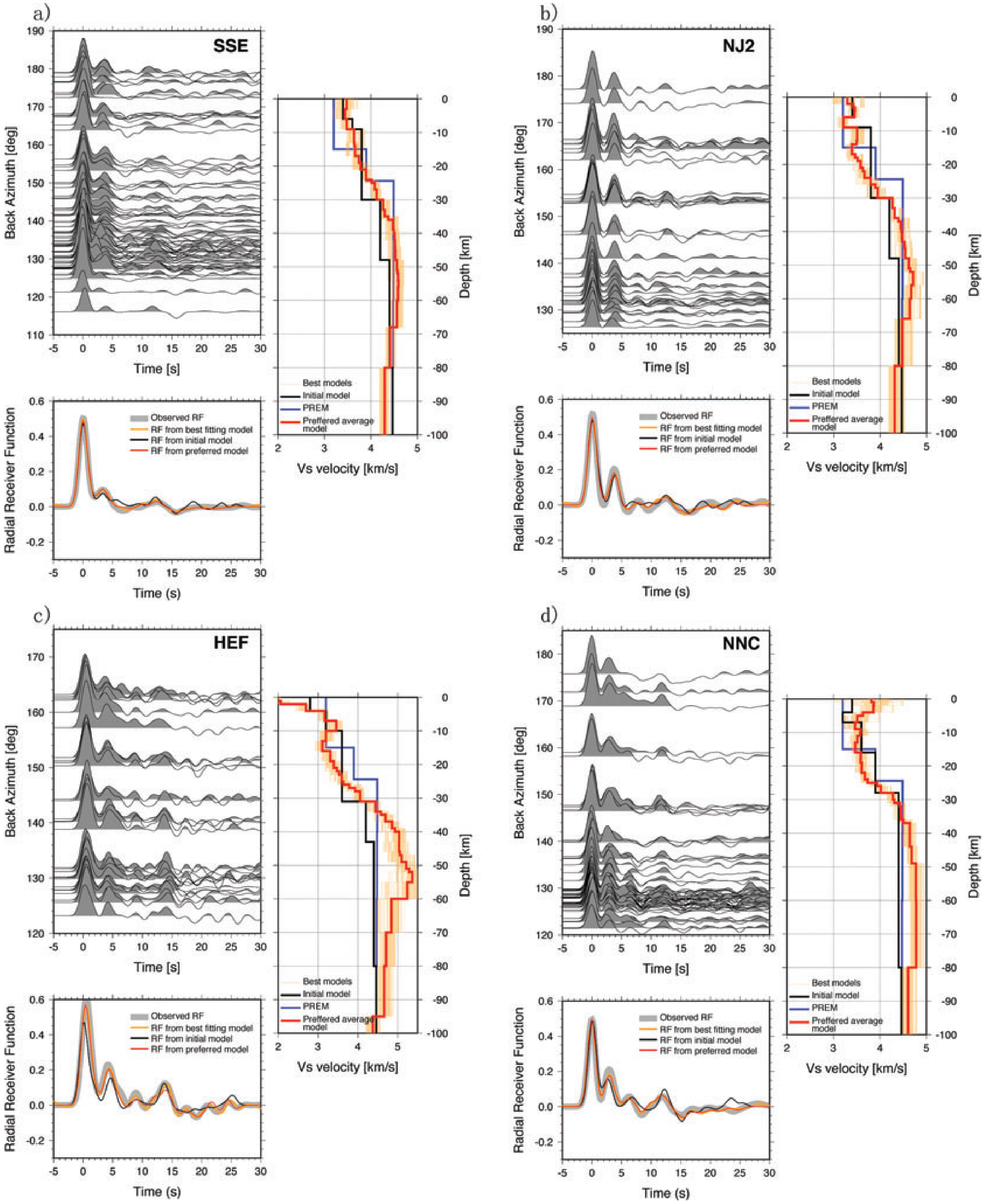

Figure 10. Same as Fig. 9, but for stations located in the Yangtze Craton: (a) SSE, (b) NJ2, (c) HEF and (d) NNC, (e) CNS, (f) WHN, (g) ENH and (h) GYA. (Continued) Same as Fig. 9, but for other four stations located in the Yangtze Craton: (e) CNS, (f) WHN, (g) ENH and (h) GYA.

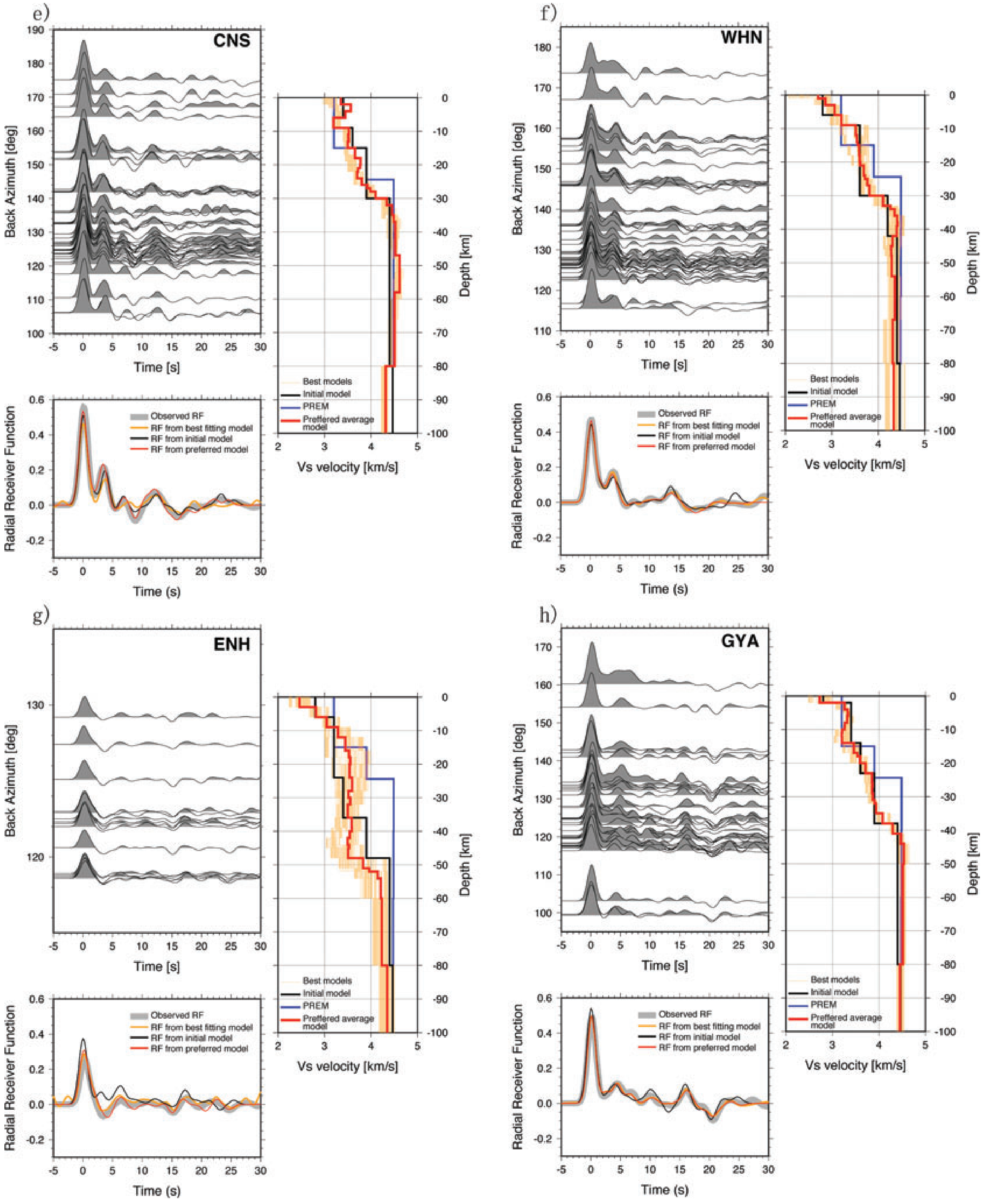

Figure 10. (*Continued.*)

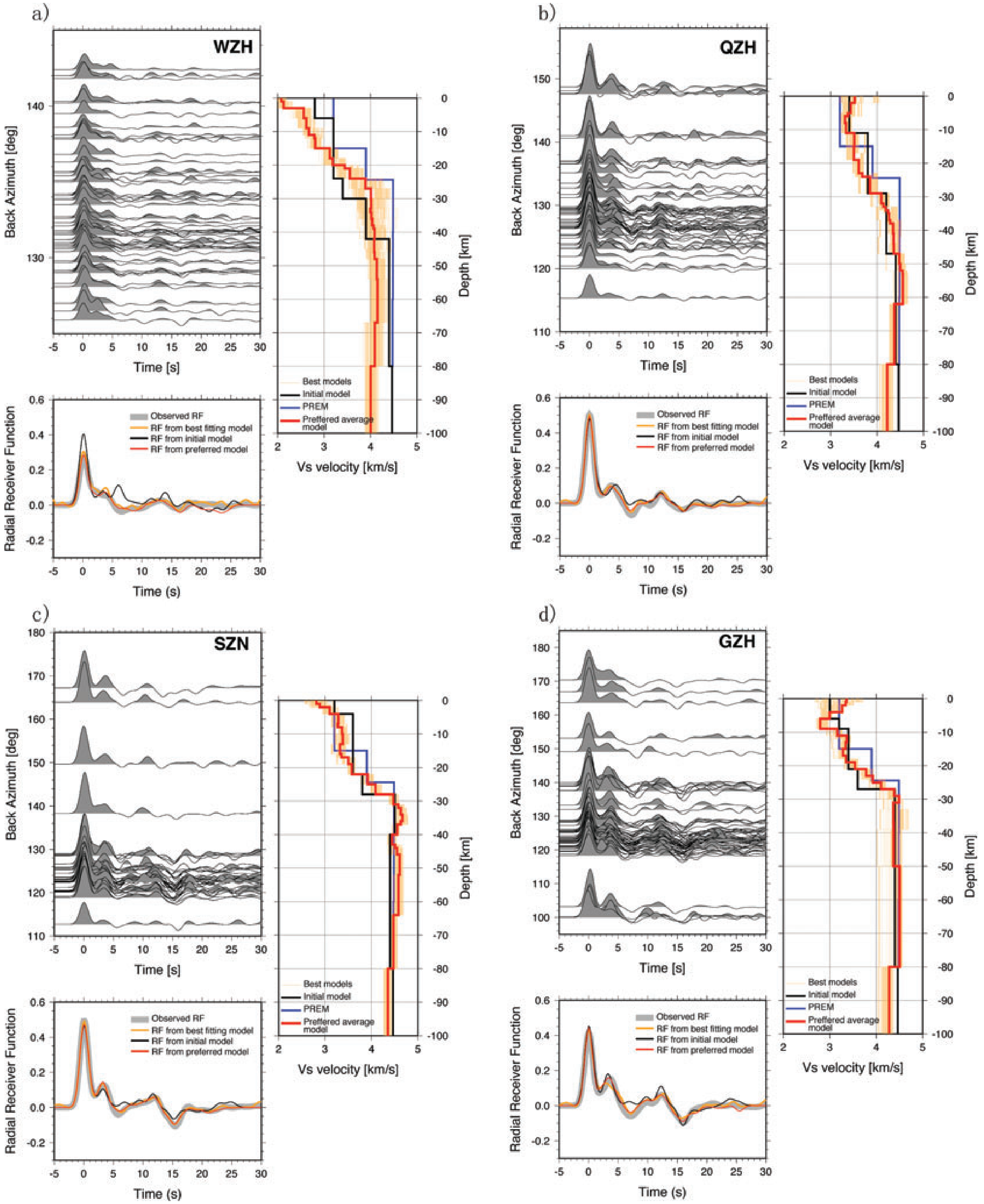

Figure 11. Same as Fig. 9, but for stations located in the South China fold system: (a) WZH, (b) QZH, (c) SZN and (d) GZH, (e) GUL and (f) QIZ.

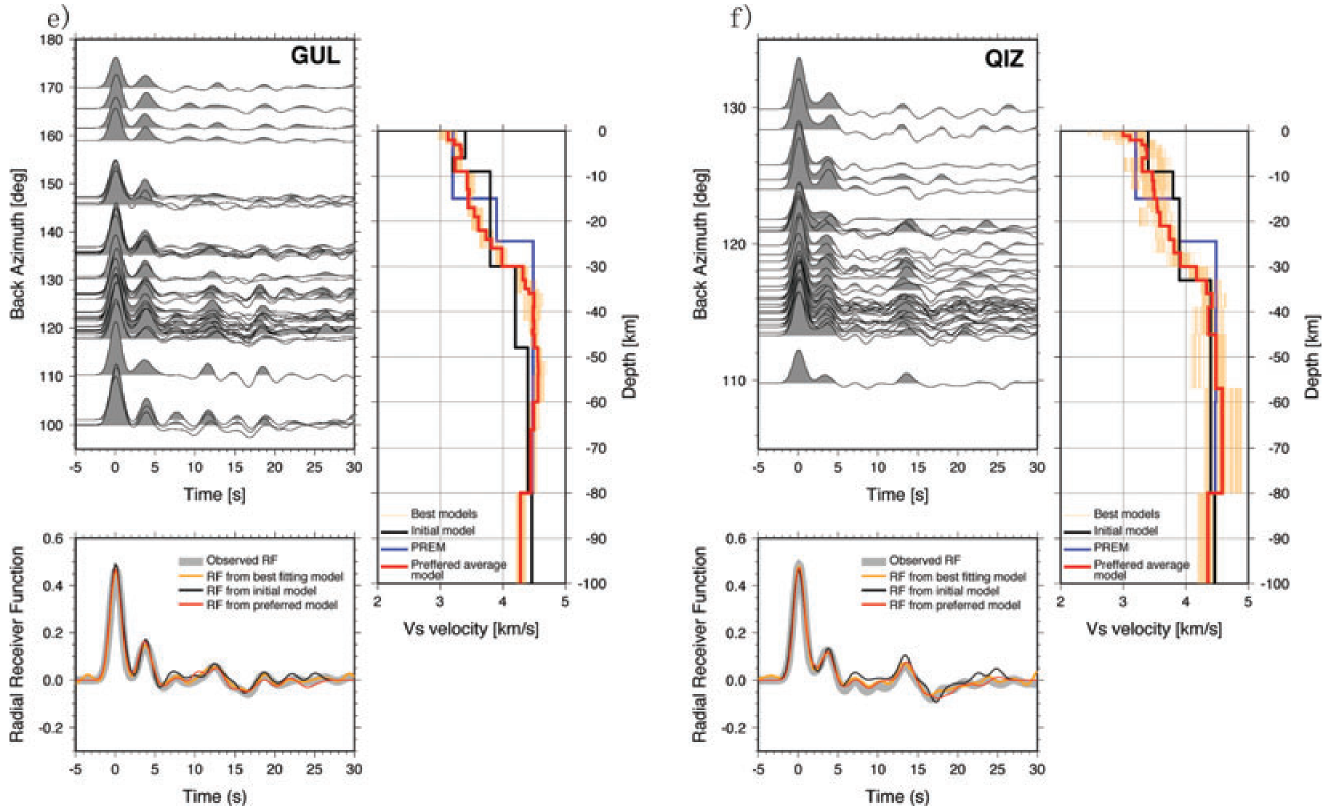

Figure 11. (*Continued.*)

and HEF are located along Qinling-Dabie fold system, but we set them to the Sino-Korean Craton and the Yangtze Craton, respectively. QIZ is on Hainan Island, and we account it as a station in the South China fold system. We first describe results of each station in the order of three major tectonic regions from the north towards the south, and we then compare our resulting Earth models to those derived from different geophysical methods.

3.1.1 The Sino-Korean Craton

Station TIA is among the highest quality stations analysed in this study, with a large number of coherent RF waveforms from all backazimuths (Fig. 9a), and would be a good candidate for a textbook example of this type of study. From our experience in analysing RFs in different parts of the world, it is very rare to see such a high percentage of mutually coherent waveforms recorded at a single station from multiple earthquakes. Both *P*-to-*S* conversions and multiples phases are clearly observed. Three different techniques result in Moho at about 32 km depth, well consistent with the results from previous tomographic studies if measurement error is considered. The crustal velocity structure is relatively simple, which can be accurately explained by a four-layer model. Specifically, a sedimentary layer at the top 2 km is followed by an upper crustal layer extending to the depth of 11 km, a middle crustal layer reaching the depth of 27 km and a lowermost crustal layer reaching the depth of 32 km, at which a sharp Moho occurs.

Station HNS has a clear 2-km thick layer of low velocity at the surface and a sharp discontinuity at 8 km (Fig. 9b). The depth of Moho, averaged over the three techniques is 32–33 km (Table 2), similar to the results of seismic tomography. The velocities in the upper mantle are higher than PREM, which was also seen for other stations such as LYN (Fig. 9c) and NJ2 (Fig. 10b). The lid-like feature obtained in the upper mantle between the depths of about 50 and 70 km.

Station LYN is located on the stable craton in north China, and has a relatively thick and well-defined crust in comparison with the above two stations, TIA and HNS (Fig. 9c). The prominent features of the Earth structure revealed beneath this station are a very sharp crust–mantle transition at about 36 km and a lid in the mantle with high shear wave velocity (about 5.0 km) between about 40 and 50 km depth. Shear wave velocities remain high throughout the uppermost part of the upper mantle. The Moho depth is estimated by averaging over all three techniques we used. Although the *H*–*κ* search generates a result consistent with previous tomographic studies, our average value shows the crustal thickness in this region thicker than that by, possibly, as much as 5 km. The *P*-to-*S* conversions are well pronounced and coherent for a wide range of backazimuths, and the multiples show complexities due to the upper mantle structure.

The above three stations all sit on the Sino-Korean Craton in north China. Their velocity profiles in the crust look similar; however, they also present apparent differences in the upper crust. Station XAN is located on the Qinling Mountain, about 330 km further inland from the nearest station LYN on the Sino-Korean Craton (Fig. 1). The relatively thick and complicated crust beneath this station makes it possibly the most difficult station to interpret. It has a very coherent peak corresponding to the *P*-to-*S* conversions, but it is evidently missing phase-multiples for all backazimuths. The resulting velocity profile is characterized by a fairly constant velocity in the top 15 km, and a gradual increase in velocities down to 50 km, without a very clear indication of where the transition between the crust and the mantle occurs (Fig. 9d). Two possible transitions occur in the lower crust: one at about 33 km and another at about 44 km. We also found two maxima values on the *H*–*κ*

Table 2. Results for the depth of Moho (and v_p/v_s ratio where estimated), with uncertainties and sharpness (0 = gradual; 1 = sharp) from three different techniques used in this study: (1) grid-search (columns 2–4), (2) inversion (columns 5–7) and (3) H–κ domain search (columns 8–11). Also shown are Moho-depths and velocities in the layers above and below Moho from tomographic studies of *P* waves (Sun & Toksöz 2006; columns 12–14) and *S* waves (Pei *et al.* 2004; columns 15–17).

Station name	Moho depth GRID SEARCH	Uncer-tainty	Sharp-ness	Moho depth INVERSION	Uncer-tainty	Sharp-ness	Moho depth H–κ METHOD	Uncer-tainty	v_p/v_s ratio	Uncer-tainty	Moho depth *P* tomo-graphy	v_p above Moho	v_p below Moho	Moho depth *S* tomo-graphy	v_s above Moho	v_s below Moho
CNS	30.0	2.0	1	32.0	1.5	1	30.7	±0.5	1.620	±0.012	33.4	6.60	7.93	33.42	3.81	4.35
ENH	36.0	2.0	0	37.0	3.0	0	46.3	±0.1	1.746	±0.004	37.3	6.61	7.96	37.40	3.85	4.36
GUL	30.0	1.0	1	30.0	2.0	1	30.6	±0.3	1.718	±0.007	33.5	6.62	8.10	33.71	3.85	4.44
GYA	38.0	1.0	1	39.0	1.5	0	38.6	±0.2	1.618	±0.008	37.5	6.63	7.98	37.32	3.85	4.34
GZH	28.0	1.0	1	30.0	1.5	1	30.3	±0.5	1.696	±0.030	33.4	6.64	7.90	33.40	3.84	4.42
HEF	34.0	0.5	1	32.0	3.0	0	33.9	±0.3	1.628	±0.011	33.7	6.69	7.94	33.70	3.99	4.39
HNS	32.0	0.5	0	34.0	1.5	0	31.6	±0.3	1.688	±0.012	33.7	6.63	7.86	33.89	3.85	4.34
LYN	36.0	1.5	1	38.0	2.0	1	32.4	±0.2	1.702	±0.008	33.4	6.62	7.90	33.77	3.96	4.45
NJ2	30.0	0.5	1	30.0	2.0	1	30.7	±0.2	1.736	±0.007	33.5	6.65	7.85	33.52	3.99	4.38
NNC	28.0	0.5	1	28.0	3.0	0	30.7	±0.5	1.576	±0.012	33.6	7.05	7.79	33.61	3.80	4.31
QZH	30.0	2.0	0	33.5	1.5	1	29.4	±0.2	1.706	±0.010	34.1	6.76	7.94	34.42	3.90	4.39
QIZ	33.0	1.5	1	31.0	1.5	1	32.0	±0.2	1.708	±0.009	32.4	6.73	7.93	32.35	3.87	4.29
SSE	31.0	1.0	0	32.0	2.0	0	32.2	±0.4	1.692	±0.018	33.3	6.66	7.86	33.33	3.90	4.35
SZN	28.0	1.0	1	29.0	1.5	1	30.3	±0.5	1.670	±0.021	34.1	6.72	7.85	34.19	3.87	4.30
TIA	32.0	0.5	0	32.0	1.5	1	32.7	±0.4	1.716	±0.014	33.5	6.65	7.87	33.47	3.84	4.34
WHN	30.0	2.0	0	31.5	1.5	1	31.6	±0.3	1.708	±0.009	33.4	6.65	7.87	33.19	3.92	4.43
WZH	28.0	3.0	0	28.0	3.0	0	32.7	±0.5	1.614	±0.017	33.1	664	7.89	32.93	3.86	4.43
XAN	44.0	2.0	0	44.0	3.0	0	38.3	±1.4	1.662	±0.017	43.3	7.26	7.94	43.32	3.85	4.32

contour map. One corresponds to a depth at 34.7 km with a higher v_p/v_s value of 1.73, whereas the other corresponds to a depth at 38.3 km but with a lower v_p/v_s value of 1.66. These two distinct crustal thickness and v_p/v_s ratio combinations could be the result of their trade-off effect. We interpret the deeper transition as the crust–mantle transition since it was also suggested by tomography. Moreover, our interpretation makes physical since the relatively low value of v_p/v_s ratio could result from a thick crust with high shear wave velocity in the lowermost layer. However, it is possible to interpret the transition at the shallower depth as Moho, as the position of the *P*-to-*S* conversion related peak suggests.

3.1.2 The Yangtze Craton

Station SSE is one of the stations along the eastern coastline (Fig. 1), characterized with less prominent, yet coherent *P*-to-*S* conversions for a wide range of backazimuths (Fig. 10a). However, multiple phases are only weakly recorded. This is most likely due to a very gradual crust–mantle transition. Moho occurs likely at around 30 km depth, but with a wide transition zone, probably as large as 5 km. The estimates of Moho depth from this inversion, the *H*–*κ* search, as well as independent tomographic studies are well within this range.

Station NJ2 is located near the Yangtze River. It has unusually clear second peaks (*P*-to-*S* conversions), but the multiples are very weak (Fig. 10b). This is most likely the consequence of a complex and inhomogeneous structure in the upper crust that causes scattering and inhibits clear observations of *PpPhs*, *PpShs* and *PsPhs* phases. The upper part of the crust has a sharp transition to a low velocity at 6 km and another sharp transition to a higher velocity at 9 km. This is followed by 5 km of constant velocity and another drop in velocities at about 15 km. For the depths below 15-km mark, velocities increase gradually down to 30 km, where a sharp Moho occurs. The Moho depth estimated from our three techniques is consistent with each other, whereas tomographic studies may overestimate crustal thickness in this area by about 3.5 km.

Station HEF is situated near station NJ2, roughly on the boundary of the NCB and SCB along the Qinling-Dabie suture zone (Fig. 1). Contrary to NJ2, crustal reverberations are well observed, thus some other features are obtained with more confidence (Fig. 10c). For example, this station appears to have a 4-km thick sediment with very low velocity, a low-velocity zone between 10 and 16 km, and a gradual increase of velocities in the lower crust, with a profile very similar to that of NJ2 station. Although not being a very sharp transition, Moho most likely occurs between the depths of 31 and 34 km, in excellent agreement with tomography results. However, the data associated with this station has a very pronounced lid of high shear velocities in the upper mantle, with a gradual increase to 5.35 km s^{-1} at 55 km and a steeper reduction to the PREM-like values at about 80 km.

Station NNC has a more complicated second peak corresponding to *P*-to-*S* conversions (Fig. 10d), which is a result of a more gradual crust–mantle transition. Moreover, crustal structure beneath this station is characterized by relatively large velocities near the surface, and a gradual decrease as a function of depth, which also contributes to the complexity of the observed RFs waveforms. This is confirmed by the interactive modelling using IRFFM. Grid-search and inversion return Moho depth at 28 km, while the *H*–*κ* method yields a slightly larger depth (30.8 km), but with an unusually low v_p/v_s ratio of 1.58 (see Table 2). It is likely that the v_p/v_s ratio is higher, and raising it taking into account a possible trade-off effect in the *H*–*κ* domain search would also decrease the depth of Moho. Thus, our results indicate about a 4–5 thinner crust under NNC, than what was obtained in tomographic studies. The upper mantle beneath this station has high shear wave velocities, reaching 4.8 km s^{-1} between the depths of 50 and 80 km.

Station CNS is characterized by a relatively sharp Moho at about 31 km depth (Fig. 10e), and a narrow low-velocity zone in the upper crust ending with a discontinuity at 9 km depth, a feature similar to that seen at other two proximate stations: GZH and GUL. RFs have a very clear *P*-to-*S* conversion for all backazimuths. Multiple picks corresponding to crustal reverberations are relatively well recorded. The depth of Moho at 31 km is the average obtained from three applied techniques, and is about 2 km shallower than that from tomographic studies.

Like NNC and CNS, station WHN is located in the central part of the Yangtze Craton (Fig. 1), about 240 km northwest from station NNC and 295 km northeast from station CNS. This station has slightly lower velocities near the surface (Fig. 10f), but apart from that, the velocity profile looks very similar to that of stations NNC and CNS. We find an average Moho at about 31 km. The *P*-to-*S* conversions and multiples are reasonably strong and constant for a wide range of backazimuths, and this gives us the confidence that the depth of Moho is well estimated by our techniques and slightly overestimated in tomographic studies (Table 2). The velocity models of stations WHN, NNC and CNS have similar pattern throughout the crust, although with some differences. For example, the more complicated second peak shown on NNC probably indicates a more gradual Moho than for station CNS.

As another station located at the centre of the Yangtze Craton, station ENH is located farther west than WHN, NNC and CNS (Fig. 1). It presents somewhat complicated structure in the crust (Fig. 10g). This probably causes the smallest number of coherent RFs suitable for further analysis. The *P*-to-*S* conversion, as well as multiples phases corresponding to the reverberation in the crust is weak, and there is some degree of coherency among them. Our modelling results in Moho at about 36–37 km, fairly consistent with the values from tomography, but the *H*–*κ* domain search shows a much larger depth at about 46 km. Interestingly, there is another sharper discontinuity present at the depth of about 48 km in the inversion model. If this depth is assumed a discontinuity in the mantle, our *H*–*κ* domain search must interpret it as Moho, but neglects the discontinuities at shallower depth.

Station GYA has relatively incoherent transitions from *P* to *S* (Fig. 10h), which is visible in the broadened character of the second peak in the observed RFs. Interactive modelling shows that the broadened waveforms are a result of a gradual Moho, but also a low-velocity zone present in the upper crust. GYA is characterized by a somewhat low velocity in the uppermost 2 km, a gradual decrease of velocity with depth and a relatively sharp discontinuity in elastic properties towards higher values at about 14 km. Moho is moderately gradual to well pronounced at about 39 km, which represents the second largest depth among all stations studied here (see Table 2). All three methods produce consistent depth of Moho, and this is also in a reasonably good agreement with tomographic studies, which found Moho at 37.5 km. The *H*–*κ* domain search produced v_p/v_s ratio of 1.62, which is some of the lowest ratio of all stations.

3.1.3 The south China fold system

WZH is a coastal station characterized by at least 2–3 km of sediments and a gradual increase of velocity with depth. Thus it has very weak, but relatively coherent conversions from *P* to *S* and some evidence of coherent multiple reverberations from all backazimuths (Fig. 11a). Consequently, it is difficult to estimate a precise Moho depth from grid-search (poor fits), inversion (gradual Moho), as well as the *H*–*κ* domain search. Although it is possible that Moho is as shallow as 25 km, our estimate of 32.7 ± 0.5 km is influenced by the tomographic studies that estimated Moho at about 33 km. Upper mantle shear velocities are significantly lower than those in PREM, reaching only 4.1 km s^{-1}.

Station QZH is also located along the eastern coast, further southwest from station WZH (Fig. 1). However, crustal structure of this station is significantly different from that of WZH, with higher absolute velocities and no visible sediments (Fig. 11b). The first peaks are not as damped as for station WZH and the *P*-to-*S* conversions are clearly seen. There is however some disagreement among the measurements for Moho depth using different methods, ranging from 29.4 km by the *H*–*κ* domain search, 33.5 km by our multistep approach, to 34 km by both tomographic methods. Immediately below Moho, upper mantle shear velocities are lower than those in PREM, but turn to slightly exceed PREM values at about 50 km.

Station SZN is a coastal station located in the vicinity of Shenzhen, only 110 km to GZH. Unlike the nearby inland station GZH (Fig. 1), it is a noisier station, and does not produce as large number of waveforms suitable for modelling as some continental stations. This station has significantly lower velocities near the surface than station GZH (Figs 11c and d). Our modelling, however, does not produce a low-velocity zone in the upper crust, which was the case for station GZH. Moho depths beneath these two stations are very similar (see Table 2). An average from the three techniques used in this study produces 29 km for the crust–mantle transition, and it seems that the transition is relatively sharp, with PREM-like velocities in the upper mantle.

Station GZH is situated in the urban area of Guangzhou and the Pearl River Delta, near the coast of the South China Sea (Fig. 1). Secondary peaks are not prominent (Fig. 11d), which might be due to pronounced inhomogeneities and attenuation in the crust. Although it was expected that the surface layers would be characterized with low velocity, the velocity gradually decreases from the surface and reaches its minimum (2.7 km s^{-1}) at about 6 km. It then remains constantly low to the depth of 9 km, where a significant discontinuity marks a transition from low to higher velocities. We conclude that Moho occurs at about 29 km, although it does not manifest itself in a sharp transition, but rather as a change in character from a steep gradient to a constant velocity as a function of depth. This Moho depth is about 3–4 km shallower than the results derived from previous tomographic studies, thus the pattern of overestimating crustal thickness seen for other stations is similar here.

As the only inland station in the region, station GUL has clearly defined *P*-to-*S* conversions for all backazimuths (Fig. 11e), as well as pronounced multiples in the range of backazimuths we considered. This station has relatively constant velocities in the upper crust, with a mild discontinuity at about 9 km depth and a very clear Moho at 30 km depth. This depth is consistently obtained from all three techniques (Table 2). Similarly to station GZH, Moho is probably overestimated in previous tomographic studies by more than 3 km.

The central part of the Hainan Island is chosen for the location of station QIZ (Fig. 1). This station has a clearly defined transition from *P* to *S* (Fig. 11f), and secondary arrivals corresponding to the crustal reverberations, which are more striking than those for the continental stations mentioned earlier. The velocity profile resembles that of a continental station, such as GUL. There is possibly a mild discontinuity at about 9 km depth. The average crustal thickness we obtain from all three techniques (the grid-search, the *H*–*κ* domain search and the linearized inversion) is 32 km. This agrees very well with the results from seismic tomography. In an independent study developing the Bayesian approach in RFs analysis (Bodin *et al.*, in preparation) we confirm this result.

4 DISCUSSION

4.1 Crustal thickness and v_p/v_s variations

We generate a 2-D map of crustal thickness by interpolating our 18 point measurements made in southeast China from the *H*–*κ* domain search (Fig. 12a) and the linearized inversion modelling (Fig. 12c) and compare it with the map of crustal thickness derived from *P*-wave tomography (Sun & Toksöz 2006, Fig. 12d). The lateral variation of crustal thickness revealed by these studies is similar. They all present a relatively thin crust to the southeast along the eastern coast, and a thick crust towards the northwest. However, our 1-D models for a number of stations on the Yangtze Craton and the South China fold system yield the crust thinner than that from tomography, suggesting that tomographic studies may overestimate crustal thickness for these tectonic regions. Specifically, the stations with reduced thickness in comparison with tomographic results may include NJ2, NNC, CNS, WHN, SZN, GZH and GUL as shown in Table 2. One has to note here that the main purpose of the 2-D map is to demonstrate lateral variations of crustal thickness and make comparison with tomographic models. It does not mean that the map based on RFs has a higher resolution and is able to reveal more structural details than tomographic model. Our 2-D interpolation emphasizes the local variation around the measurement at each point, while the tomography focuses on averaged and smoothed effects over the entire path-coverage area.

The results of the v_p/v_s ratio from our *H*–*κ* domain search method are plotted in Fig. 12(b). We have recently made improvements in our measurements, and therefore the results presented in Fig 12(b) are slightly different from those presented in Chen *et al.* (2010, their fig. 7). In particular, v_p/v_s ratio for the coastal station WZH in the South China fold system is reduced to 1.61 (Table 2), whereas in Chen *et al.* (2010), this value was as high as 1.88. Another significant change is the reduction of v_p/v_s ratio for station HEF (the border between the Sino-Korean and the Yangtze cratons) from 1.72 to 1.63 (Table 2).

The v_p/v_s ratios are important in revealing the mineralogical composition of the crust. Although we do not find any obvious correlation between the crustal thickness (or age) and v_p/v_s ratios (e.g. stations WHN and NNC have similar crustal thicknesses, but very different v_p/v_s ratios), we can conclude that the v_p/v_s ratios for the entire region of study are very small, ranging from 1.576 (NNC) to only 1.746 (ENH). This is much smaller than the global average of 1.84 for shields and platforms (Zandt & Ammon, 1995). Relatively small values of v_p/v_s ratios that we observe in the southeast part of China could be a result of a combination of a large-scale delamination event responsible for the removal of mafic layer from the lower crust (hence reducing v_p/v_s ratios) and the presence of silicic sediments (further reducing v_p/v_s ratios), as suggested in Chen *et al.* (2010).

On the one hand, the lack of correlation (or anticorrelation) between the crustal thickness and v_p/v_s ratios is in agreement with the conclusions of Chen *et al.* (2010) for the entire mainland China. On

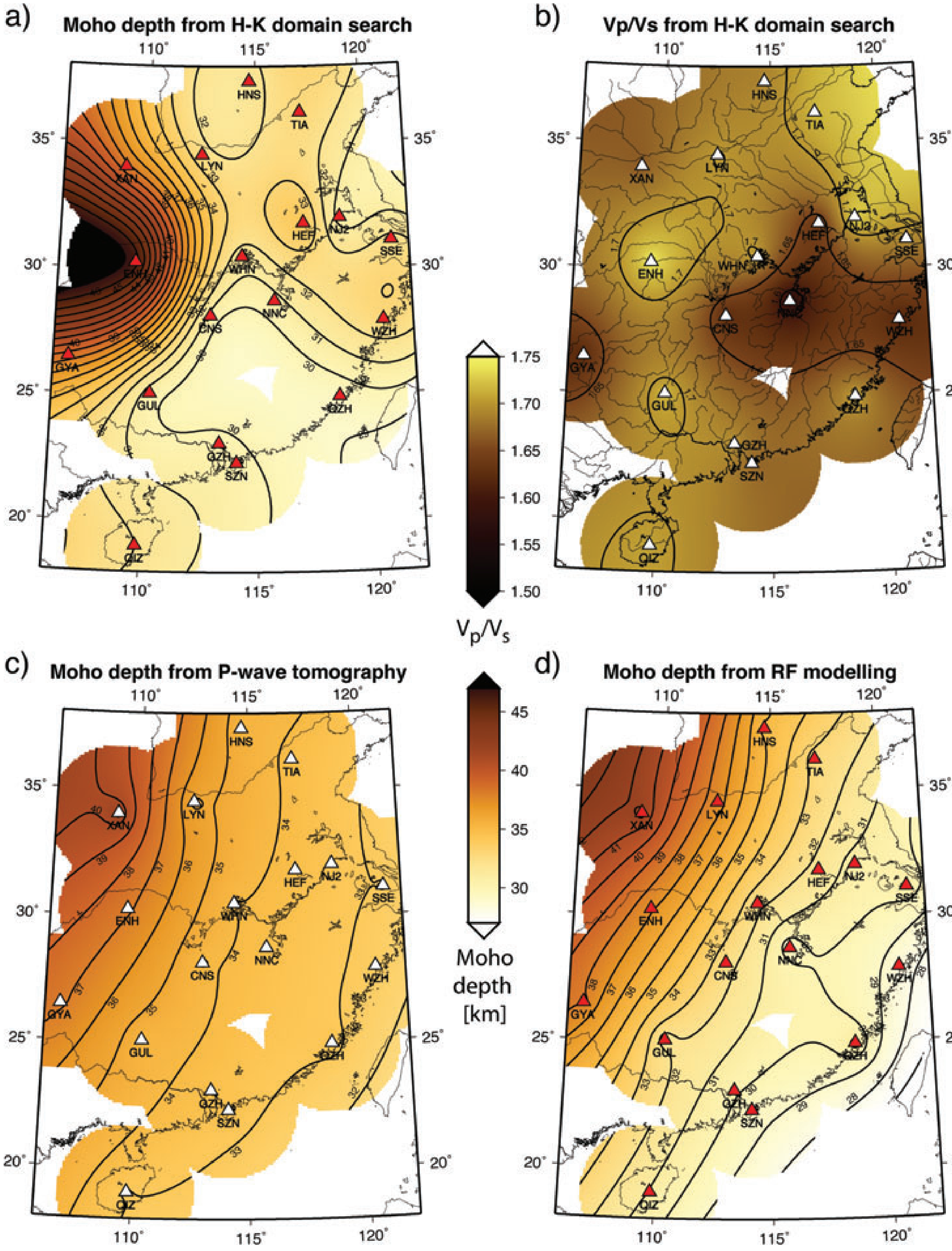

Figure 12. Comparison of interpolated maps of crustal thickness (Moho depth) and v_p/v_s ratio for southeast China using 18 data points corresponding to the locations of the stations from this study. (a) Moho depth from the H–κ domain search (Chen *et al.,* 2010 values modified) shown in column 8 of Table 2, (b) v_p/v_s ratio from the H–κ domain search (Chen *et al*., 2010 values modified) shown in column 10 of Table 2, (c) Moho depth from P-wave tomography (Sun & Toksöz 2006) shown in column 12 of Table 2 and (d) Moho depth from this study, using RFs inversion modelling results shown in column 5 of Table 2.

the other hand, our findings are mainly different from the results of Chevrot & van der Hilst (2000), who found linear trends between the crustal thickness and v_p/v_s ratios for the Australian crust. However, they also found a bimodal distribution for the Archean crust, similar to our results (see values in Table 2 for stations ENH, GYA and NNC from the Yangtze Craton), although with considerably higher range of v_p/v_s ratios. The relationship between the age of the crust and v_p/v_s ratios is a controversial topic. Durrheim & Mooney

(1994) found that the Proterozoic terranes in general have a thicker crust than the Archean, whereas Zandt & Ammon (1995) found that v_p/v_s ratios in general increase with the age of the crust. In the southeast part of China, we do not observe any systematic variation in v_p/v_s ratios within the same geological unit.

4.2 Comparison with previous studies

Wang *et al.* (2000) studied a seismic refraction profile which started from the Hefei Basin of the Sino-Korean Craton and extended to the Yangtze Craton across the Dabie orogenic belt with a N25°E trend. Stations HEF and NNC are located at the northern and southern end of the profile, respectively, and NJ2 and WHN are about 150 km away from the profile on the eastern side and western side, respectively. Over the entire 400-km long seismic profile, this study determined a 2-D *S*-wave model with monotonically increasing velocities with depth. Comparing the sample of the Sino-Korean Craton close to HEF with the sample of the Yangtze Craton close to NNC, we conclude that the *S*-wave velocities change: (i) from 3.57 to 3.41 km s^{-1} in the upper crust down to about 18 km excluding sedimentary layer; (ii) from 3.72 to 3.62 km s^{-1} in the middle crust down to about 26 km and (iii) from 3.79 to 3.84 km s^{-1} in the lowermost crust down to Moho at about 35 km. The crustal thickness beneath these four stations obtained from our RF analysis is between 30 and 33 km, a few kilometres thinner than the active-source estimates for two cratonic blocks. The average values of *S*-wave velocities shown in our RF models are roughly within the range of the deep seismic sounding (DSS) study, but the structural details are quite different, probably reflecting more local structure beneath each station. The DSS model has a sedimentary layer of 2–5 km thick along the entire profile. However, only HEF has a 2-km thick sedimentary layer, as we would expect based on the location in the Hefei Basin. The crustal structure beneath HEF and NJ2 can be characterized as gradually increasing *S*-wave velocity with a prominent low-velocity zone between 10 and 20 km, which was not revealed in the DSS model. The crustal structure beneath NNC and WHN is relatively simple, suitable to be modelled by several layers with a uniform *S*-wave velocity in each layer. They are more consistent with the DSS models than HEF and NJ2 stations. A clear discontinuity at 9 km in the WHN model does not stand out in other stations or in the seismic profiles, which implies a local structure around WHN.

Another seismic profile deployed in south China runs in the NW–SE direction from Tunxi, Anhui province to Wenzhou, Zhejiang province across several major active faults and basins. Zhang *et al.* (2005) analysed the wide-angle reflected seismic data collected in this profile to determine 2-D *P*- and *S*-wave crustal models. The average crustal thickness along this profile is about 36 km with gradually thinning from northwest to southwest as the Moho depth decreases. Station WZH is located at the southeastern end of this profile, and the three techniques used here estimate crustal thickness of 28–33 km (Table 2). These values are compatible with the 31–32 km identified in a profile for the southeastern end. We note that the primary *P*-to-*S* converted phase is relatively weak on the RFs of WZH compared to the crustal multiple phases, which may be associated with irregular scattering from Moho topography. It suggests that the crust–mantle boundary is not a simple discontinuity in velocity, but a transition zone enhanced by a strong velocity gradient. The same conclusion was also obtained from this profile by the observation of multiple refracted *Pn* and *Sn* phases clustered after the *Pm* and *Sm* arrivals. It is found from this profile that a low-velocity layer of about 4 km thick with *S*-wave velocity of 3.5 km s^{-1} marks the bottom of the middle crust at a depth of 23 km northwest and 17 km southeast. However, such a low-velocity zone does not exist in our model of WZH through the crust.

One important geoscience transect in China runs from Menyuan, Qinghai province northwest to Ningde, Fujian province southeast with a total length of 2200 km. The east section of this geoscience transect crosses our study region, and reflects the rifting and extension of the western Pacific Ocean generating a series of extensional faults and rifted basins, and thinning the lithosphere and crust. At least two stations, XAN and WHN, are located along this geoscience transect. Wang *et al.* (1995) outlined the geophysical results based on two DSS profiles along this transect. They concluded that the crust under the Qinling fold system has a thickness of 35 km and a relatively low *S*-wave velocity, whereas the crust begins to thin out with relatively high *S*-wave velocity when the transect extends to the Dabie mountains, Yangtze Craton, and south China fold system. The RF model beneath XAN implies a thick crust with relatively complicated structure. It is difficult to explicitly determine where the transition between the crust and the mantle occurs. However, WHN displays relatively simple crustal structure and small thickness compared to XAN. Our modelling shows that the average crustal *S*-wave velocity beneath WHN is about 0.2 km s^{-1} higher than that beneath XAN.

We made a superficial comparison of the crustal structure derived from different types of seismic studies. Some general features in crustal structure are in good agreement among different techniques. The detailed crustal structure, however, presents considerable discrepancy among these techniques. This is probably due to the fact that the DSS models, as well as tomographic models pursue a smoothed structure over their 2-D or 3-D study areas, whereas RF focuses on local structure beneath individual stations. The discrepancy for crustal thickness could be caused by different definitions of the Moho and different sampling nature in active and passive seismic data. As the active-source and RF data cover very different frequency bands, the consistency in crustal thickness estimates indicates that the Moho beneath these stations must be a sharp boundary with a thickness of less than 2 km. If the crust–mantle transition occurs gradually, the estimated Moho depth depends on the wavelength of the sampling waves. While high-frequency active-source data more or less report the depth associated with a rapid change in velocity, the long-wavelength teleseismic waves are likely to give the average depth of the entire transition. Also, active-source reflection data sample the Moho from the upper side, whereas RFs primary wave illuminates the boundary from the lower side. Moreover, the arrivals of *S* waves are difficult to be picked in comparison with the arrivals of *P* waves, because either they are not well developed in DSS experiments or they are buried in *P*-wave coda. Thus, *S*-wave velocity models are not as reliable as *P*-wave velocity models in these active seismic source experiments.

5 CONCLUDING REMARKS

We introduced and applied an IRFFM software to model RFs observed at 18 broad-band stations from the southeast part of China. The software is made freely available on the Internet. We also presented a method for isolating only mutually coherent RFs from a large stack of RFs, which is based on computing a cross-correlation matrix and an empirical determination of a couple of parameters. Upon analysing RFs with IRFFM, three steps: the H–κ domain search, a grid-search and a linearized inversion were conducted at different stages of a multistep approach to the modelling of Earth structure. This multistep approach is time consuming, but presents a reliable way of understanding all intricacies of Earth structure that we attempt to model.

To complement information from the observed RFs on the gradients in elastic parameters, and to increase constraints on absolute velocity structure, we used the existing *P*-wave (Sun & Toksöz 2006) and *S*-wave (Pei *et al.* 2004) tomography models. We modified our starting models from IRFFM and grid-search before the inversion procedure using tomographic absolute velocities from the layers above and below Moho, as well as the v_p/v_s ratio from the H–κ domain search. By doing so, we ensured that the resulting models were compatible with various sets of observations, in a similar fashion to that done in joint inversions of multiple geophysical data sets. This is important in the context that the solutions in linear inversions are easily trapped in local minima, and therefore final models are strongly dependent on initial models.

The observed crustal thickness has apparent lateral variation across our study region. The thinnest crust lies along the coast of the South China fold system and the Yangtze Craton. It gradually thickens by more than 10 km towards the northwest and northeast. The estimates of crustal thickness beneath the Yangtze Craton and the South China fold system from RFs are about 3–5 km lower than those from teleseismic tomography. This difference is not surprising, given the limitations in vertical resolution known in teleseismic tomography.

We observed predominantly small values of v_p/v_s ratios across the entire region, which could be caused by a combination of a large-scale delamination event responsible for the removal of mafic layer from the lower crust, and the presence of silicic sediments, both reducing v_p/v_s ratios in the crust, as suggested in Chen *et al.* (2010). We did not observe any correlated (or anticorrelated) variation of crustal thickness or age of the crust with v_p/v_s ratios, suggesting that simple relationships between mineralogical composition and crustal thickness and age are not a global feature of the Earth's crust.

Although our study region covers a large area of Archean cratons, the underlain crustal structure is not simple, given the long history of evolution of the North and South China blocks. The widely spread basins, mountains and uplifts result in diversity of local crustal structure, which is revealed by the difference of velocity models under nearby stations such as HEF and NJ2, and GZH and SZN. The *S*-wave velocity models of some stations across all three tectonic blocks display a low-velocity zone (such as NJ2, HEF, CMS, GYA, GZH and GUL) in the upper crust and a discontinuity at about 9–10 km (such as HNS, NJ2, CNS and WHN). These features could reflect local crustal structure around individual stations or a small area, but it would be too ambitious to relate them to geology and tectonics. On the one hand, some stations have simple, PREM-like structure in the mantle. On the other hand, there are a number of stations to the east and southeast of our study region with a feature in the upper mantle resembling a lid with high *S*-wave velocities. It probably reflects a general property of upper mantle structure of the eastern part of the North and South China blocks.

Last but not least, this study demonstrates that multiple geophysical data for crustal thickness, average v_p/v_s ratio and lower crust and upper mantle velocities can be successfully combined from independent data sets to construct crust and upper mantle profiles, in this case, for southeast China. It is hoped that the next generation of lithospheric images of this part of China will use crustal profiles derived in this study as a useful *a priori* constraint.

ACKNOWLEDGMENTS

We would like to thank to the authors of Generic Mapping Tools (GMT) software (Wessel & Smith 1998). We also thank C. Ammon for making his iterative inversion code available from http://eqseis.geosc.psu.edu/~cammon/HTML/RftnDocs/rftn01.html.

REFERENCES

Agostinetti, N.P., Lucente, F.P., Selvaggi, G. & Di Bona, M., 2002. Crustal structure and Moho geometry beneath the northern Appennines (Italy), *Geophys. Res. Lett.,* **29**(20), 1999, doi:10.1029/2002GL015109.

Ammon, C.J., 1991. The isolation of receiver effects from teleseismic P waveforms, *Bull. seism. Soc. Am.,* **81,** 2504–2510.

Ammon, C.J., 1997. *Receiver-Function Inversion,* software and manual available at http://eqseis.geosc.psu.edu/~cammon/HTML/RftnDocs/rfinv01.html (last accessed 2010 September 12).

Ammon, C.J., Randall, G.E. & Zandt, G., 1990. On the non-uniqueness of receiver function inversions, *J. geophys. Res.,* **95,** 15 303–15 318.

Baker, G.E., Minster, B., Zandt, G. & Gurrola, H., 1996. Constraints on crustal structure and complex Moho topography beneath Piñon Flat, California, from teleseismic RFs, *Bull. seism. Soc. Am.,* **86,** 1830–1844.

Birch, F., 1961. The velocity of compressional waves in rocks to 10 kilobars, Part 2, *J. geophys. Res.,* **66,** 2199–2224.

Çakir, Ö., Erduran, M., Çinar, H. & Yilmaztürk, A., 2000. Forward modeling RFs for crustal structure beneath station TBZ (Trabzon, Turkey), *Geophys. J. Int.,* **140,** 341–356.

Cassidy, J.F., 1992. Numerical experiments in broadband receiver function analysis, *Bull. seism. Soc. Am.,* **82,** 1453–1474.

Chang, S-J., Baag, C-E. & Langston, C.A., 2004. Joint analysis of teleseismic RFs and surface wave dispersion using the genetic algorithm, *Bull. seism. Soc. Am.,* **94,** 691–704.

Chen, Y., Niu, F., Liu, R., Huang, Z., Tkalčić, H., Sun, L. & Chan, W., 2010. Crustal structure beneath China from receiver function analysis, *J. geophys. Res*., **115,** B033067, doi:10.1029/2009JB006386.

Chevrot, S. & van der Hilst, R.D., 2000. The Poisson ratio of the Australian crust: geological and geophysical implications, *Earth planet. Sci. Lett.,* **183,** 121–132.

Du, Z.J. & Foulger, G.R., 1999. The crustal structure beneath the northwest fjords, Iceland, from RFs and surface waves, *Geophys. J. Int.,* **139,** 419–432.

Durrheim, R.J. & Mooney, W.D., 1994. Evolution of the Precambrian lithosphere: seismological and geochemical constraints, *J. geophys. Res.,* **99,** 15 359–15 374.

Dziewonski, A.M. & Anderson, D.L., 1981. Preliminary reference Earth model, *Phys. Earth planet. Inter.,* **25,** 297–356.

Hearn, M.T. & Ni, F., 2000. Tomography and location problems in China using regional travel-time data, in *Proceedings of the 22nd Annual DoD/DOE Seismic Research Symposium*, US Department of Defence, Dules, VA.

Helffrich, G., 2006. Extended-time multitaper frequency domain cross-correlation receiver-function estimation, *Bull. seism. Soc. Am.,* **96,** 344–347, doi:10.1785/0120050098.

Ji, X. & Coney, P.J., 1985. Accreted terrains in China, in *Tectonostratigraphic Terranes of the Circum-Pacific Region,* Earth Sci. Ser. Vol. 1, pp. 349–361, ed. Howell, D.G., Am. Assoc. Pet. Geologists, Tulsa, OK.

Julià, J., Ammon, C.J., Herrmann, R.B. & Correig, A.M., 2000. Joint inversion of receiver function and surface wave dispersion observations, *Geophys. J. Int.,* **143,** 1–19.

Julià, J., Ammon, C.J. & Herrmann, R.B., 2003. Lithospheric structure of the Arabian shield from the joint inversion of RFs and surface wave dispersion, *Tectonophysics,* **371,** 1–21.

Kennett, B.L.N., 1983. *Seismic Wave Propagation in Stratified Media,* ch. 9, Cambridge University Press, Cambridge.

Kind, R., Kosarev, G.L. & Petersen, N.V., 1995. RFs at the stations of the German Regional Seismic Network (GRSN), *Geophys. J.,* **121,** 191–202.

Langston, C.A., 1979. Structure under Mount Rainier, Washington, inferred from teleseismic body waves, *J. geophys. Res.,* **84,** 4749–4762.

Laske, G., Masters, G. & Rief, C., 2000. http://igppweb.ucsd.edu/∼gabi/crust2.html (last accessed 2010 September 12).

Lawrence, J.F. & Wiens, D.A., 2004. Combined receiver-function and surface wave phase-velocity inversion using a niching genetic algorithm: application to Patagonia, *Bull. seism. Soc. Am.,* **94,** 977–987.

Li, S.L. & Mooney, W.D., 1998. Crustal structure of China from deep seismic sounding profiles, *Tectonophysics,* **288,** 105–113.

Li, S.L., Mooney, W.D. & Fan, J., 2006. Crustal structure of mainland China from deep seismic sounding data, *Tectonophysics,* **420,** 239–252.

Liang, C., Song, X. & Huang, J., 2004. Tomographic inversion of Pn travel times in China, *J. geophys. Res.,* **109,** B11304, doi:10.1029/2003JB002789.

Ligorría, J.P. & Ammon, C.J., 1999. Iterative deconvolution and receiver function estimation, *Bull. seism. Soc. Am.,* **89,** 1395–1400.

Ma, Y. & Zhou, H., 2007. Crustal thicknesses and Poisson's ratios in China by joint analysis of teleseismic RFs and Rayleigh wave dispersion, *Geophys. Res. Lett.,* **34,** L12304, doi:10.1029/2007GL029848.

Nair, S.K., Gao, S.S., Liu, K.H. & Silver, P.G., 2006. Southern African crustal evolution and composition: constraints from receiver function studies, *J. geophys. Res.,* **111,** B02304, doi:10.1029/2005JB003802.

Niu, F. & James, D.E., 2002. Fine structure of the lowermost crust beneath the Kaapvaal Craton and its implications for crustal formation and evolution, *Earth planet. Sci. Lett.,* **200,** 121–130.

Niu, F., Bravo, T., Pavlis, G., Vernon, F., Rendon, H., Bezada, M. & Levander, A., 2007. Receiver function study of the crustal structure of the southeastern Caribbean plate boundary and Venezuela, *J. geophys. Res.,* **112,** doi:10.1029/2006JB004802.

Owens, T.J., 1987. Crustal structure of the Adirondacks determined from broadband teleseismic waveform modeling, *J. geophys. Res.,* **92,** 6391–6401.

Owens, T.J., Taylor, S.R. & Zandt, G., 1987. Crustal structure at regional seismic test network stations determined from inversion of broadband teleseismic P waveforms, *Bull. seism. Soc. Am.,* **77,** 631–632.

Özalaybey, S., Savage, M.K., Sheehan, A.F., Louie, J.N. & Brune, J.N., 1997. Shear-wave velocity structure in the northern basin and range province from the combined analysis of RFs and surface waves, *Bull. seism. Soc. Am.,* **87,** 183–189.

Park, J. & Levin, V., 2000. RFs from multiple-taper spectral correlation estimates, *Bull. seism. Soc. Am.,* **90,** 1507–1520.

Pasyanos, M., Tkalčić, H., Gök, R. & Rodgers, A., 2007. Seismic structure of Kuwait from joint inversion of surface wave group velocities and RFs, *Geophys. J. Int.,* **170,** 299–312.

Pei, S., Xu, Z. & Wang, S., 2004. Sn wave tomography of the uupermost mantle beneath the China continent and adjacent regions, *Chin. J. Geophys.,* **47,** 250–256 (in Chinese).

Reading, A., Kennett, B.L.N. & Sambridge, M., 2003. Improved inversion for seismic structure using transformed, S-wavevector RFs: removing the effect of the free surface, *Geophys. Res. Lett.,* **30,** doi:10.1029/2003GL018090.

Sambridge, M., 1999. Geophysical inversion with a neighbourhood algorithm–II. appraising the ensemble, *Geophys. J. Int.,* **38,** 727–746.

Sandvol, E., Seber, D., Calvert, A. & Barazangi, M., 1998. Grid-search modeling of RFs: implications for crustal structure in the Middle East and North Africa, *J. geophys. Res.,* **103,** 26 899–26 917.

Shibutani, T., Sambridge, M. & Kennett, B.L.N., 1996. Genetic algorithm inversion for RFs with application to crust and uppermost mantle structure beneath Eastern Australia, *Geophys. Res. Lett.,* **23,** 1829–1832.

Sun, Y. & Toksöz, M.N., 2006. Crustal structure of China and surrounding regions from P-wave traveltime tomography, *J. geophys. Res.,* **111,** B03310, doi:10.1029/2005JB003962.

Sun, Y.S., Li, X., Kuleli, S., Morgan, F.D. & Töksoz, M.N., 2004. Adaptive moving window method for 3-D P-velocity tomography and its application in China, *Bull. seism. Soc. Am.,* **94,** 740–746.

Tkalčić, H. & Banerjed, D., 2009. *Interactive Receiver Function Forward Modeler (IRFFM),* software and manual available at http://rses.anu.edu.au/∼hrvoje/IRFFMv1.1.html (last accessed 2011 August 1).

Tkalčić, H., Pasyanos, M., Rodgers, A., Gök, R., Walter, W. & Al-Amri, A., 2006. A multi-step approach in joint modelling of surface wave dispersion and teleseismic RFs: implications for lithospheric structure of the Arabian peninsula, *J. geophys. Res.,* **111,** B11311, doi:10.1029/2005JB004130.

Vermeesch, P., 2003. A second look at the geologic map of China: the 'Sloss approach', *Int. Geol. Rev.,* **45,** 119–132.

Vinnik, L.P., 1977. Detection of waves converted from P to SV in the mantle, *Phys. Earth. planet. Inter.,* **15,** 39–45.

Wang, C.-Y., Lin, Z.-Y. & Chen, X.-B., 1995, Comprehensive study of geophysics on geoscience transect from Menyuan, Qinghai province, to Ningde, Fujian province, China, *ACTA Geophy. Sinica*, **38**(5), 590–597 (in Chinese).

Wang, C.-Y., Zeng, R.-S., Mooney, W.D. & Hacker, B.R., 2000. A crustal model of the ultrahigh-pressure Dabie Shan orogenic belt, China, derived from deep seismic refraction profiling, *J. geophys. Res.,* **105**(B5), 10 857–10 869.

Wang, Y., Houseman, G.A., Lin, G., Guo, F., Wang, Y.-J., Fan, W.-M. & Chang, X., 2005. Mesozoic lithospheric deformation in the North China block: numerical simulation of evolution from orogenic belt to extensional basin system, *Tectonophysics,* **405,** 47–63.

Wessel, P. & Smith, W.H.F., 1998, New, improved version of the Generic Mapping Tools Released, *EOS, Trans. AGU,* **79,** 579.

Yin, A. & Nie, S.Y., 1996. A Phanerozoic palinspastic reconstruction of China and its neighboring regions, in *The Tectonic Evolution of Asia,* pp. 442–485, eds Yin, A. & Harrison, T.M., Cambridge University Press, NY.

Zandt, G. & Ammon C.J., 1995. Continental crust composition constrained by measurements of crustal Poisson's ratio, *Nature,* **374,** 152–154.

Zhang, Z.M., Liu, J.G. & Coleman, R.G., 1984. An outline of the plate tectonics of China, *Bull. geol. Soc. Am.,* **95,** 295–312.

Zhang, Z., Badal J., Li Y., Chen Y., Yang L. & Teng J., 2005. Crust-upper mantle seismic velocity structure across Southeastern China, *Tectonophysics,* **395,** 137–157.

Zhou, L., Chen, W-P. & Özalaybey, S., 2000. Seismic profiles of the Central Indian Shield, *Bull. Seism. Soc. Am.,* **90,** 1295–1304.

Zhu, L. & Kanamori, H., 2000. Moho depth variation in southern California from teleseismic RFs, *J. geophys. Res.,* **105,** 2969–2980.